The Cryosphere Discuss., 6, 1781–1837, 2012
www.the-cryosphere-discuss.net/6/1781/2012/
doi:10.5194/tcd-6-1781-2012


The Cryosphere Discussions



# Radar diagnosis of the subglacial conditions in Dronning Maud Land, East Antarctica

**S. Fujita[1], P. Holmlund[2], K. Matsuoka[3], H. Enomoto[4,1], K. Fukui[1,*], F. Nakazawa[1], S. Sugiyama[5], and S. Surdyk[1]**

[1]National Institute of Polar Research, Research Organization of Information and Systems, Tokyo, Japan
[2]Department of Physical Geography and Quaternary Geology, Stockholm University, SE-106 91 Stockholm Sweden
[3]Norwegian Polar Institute, Tromsø, Norway
[4]Kitami Institute of Technology, Kitami, Japan
[5]Institute of Low Temperature Science, Hokkaido University, Sapporo, Japan
[*]now at: Tateyama Caldera Sabo Museum, Toyama, Japan

Received: 19 April 2012 – Accepted: 4 May 2012 – Published: 24 May 2012

Correspondence to: S. Fujita (sfujita@nipr.ac.jp)

Published by Copernicus Publications on behalf of the European Geosciences Union.







## Abstract

In order to better understand the spatial distribution of subglacial environments, ground-based radar sounding data for a total distance of ~3300 km across Dronning Maud Land, East Antarctica, were analyzed. The relationship between geometrically corrected bed returned power $[P^{c}_{bed}]_{dB}$ in decibels and ice thickness $H$ was examined. When $H$ is smaller, $[P^{c}_{bed}]_{dB}$ was found to decrease simply with increasing $H$, which is explicable by the thickness variation of dielectric attenuation. However, an anomalous increase in $[P^{c}_{bed}]_{dB}$ at larger $H$ occurred, which was independent of the choice of radar frequencies or radar-pulse widths. We suggest that the existence of water at the ice/substrate interfaces at larger $H$ caused this anomalous increase. We herein propose a new analytical method using these features to delineate frozen and temperate bed areas. Approximately two-thirds of the investigated area was found to have a temperate bed. Basal melting tends to occur when $H$ is larger and the surface elevation is lower. In other words, beds inland of the ice sheet tend to be temperate, with the exception of subglacial high mountains. In contrast, beds of coastal areas tend to be frozen, with the exception of fast-flowing ice at subglacial lowland or troughs. These observations suggest that subglacial water is dominantly produced at the bed of wide inland plateau and that the water is discharged to the sea dominantly through a bed of fast-flowing ice. We also found that a 20-km-wide bed in the subglacial high mountains of an inland plateau near Dome Fuji is frozen, suggesting the existence of very old ice above the bed.

## 1 Introduction

Subglacial environments of polar ice sheets are characterized by mass and energy transfers between the ice and its substrate of water, bedrock, air, or sediment. Determining the distribution of water at the ice-sheet bed is important in many fields of polar science (e.g., Priscu et al., 2008; Rémy et al., 2003; Siegert et al., 2011). For





TCD
6, 1781–1837, 2012



example, subglacial melting is an important component of mass loss in the mass balance of the ice sheet. In addition, the existence of subglacial water can influence the ice/substrate interfaces and hence modulate the dynamic behaviour of ice sheets. It has been suggested that as much as 90 % of the discharge from the Antarctic ice sheet is drained through a small number of fast-moving ice streams and outlet glaciers fed by catchment areas (e.g., Bamber et al., 2006, 2000; Bennett, 2011; Pattyn et al., 2005; Rignot et al., 2011). These studies have shown that the major ice stream systems have complex systems of tributaries that extend far inland. Rignot et al. (2011) reported nearly complete measurements and maps of ice flows for the entire Antarctic continent. They demonstrated that these features correspond neither to topographical features nor to the magnitude of the gravitational force and the expected rate of viscous flow. Instead, the features revealed that the controlling factor is the variation of slipperiness of the substrate. In this context, better understanding the slipperiness of the ice/substrate boundaries is a major step to understanding the Antarctic ice flow. Moreover, from the viewpoint of microbiology, the existence and distribution of melt water is key to understanding the habitats of microbes. Furthermore, the international ice core community assessed that ice core records for up to 1.5 Ma ago would be a major step forward (Wolff et al., 2006; Jouzel and Masson-Delmotte, 2010). For future site selection, significant preliminary information of subglacial environments from a broad area of Antarctica is expected.

Several approaches have been developed in an attempt to better understand the subglacial conditions of the ice sheet. One of these approaches is numerical modelling of the ice sheet thermodynamics with a priori information of the ice sheet (Pattyn, 2010). Based on sensitivity experiments, Pattyn (2010) estimated that 55 % of the grounded part of the Antarctic ice sheet is at the pressure melting point. Clearly, our knowledge can be increased by a combination of modelling and observational approaches. At present, major uncertainties concerning the subglacial environments are related to the temperature field, due to an insufficient knowledge of geothermal heat flow (Pattyn, 2010). This uncertainty of the temperature field affects accurate





TCD
6, 1781–1837, 2012



determination of the basal reflectivity of the radio waves and basal melting. Pattyn (2010) reported that information on observed zones of melt water production is necessary for improved basal temperature estimates.

One observational approach is to detect features of subglacial lakes from remote sensing data and compile inventories of these features (Carter, 2007; Popov and Masolov, 2007; Siegert et al., 2005; Smith et al., 2009). In addition, several studies have analyzed the reflectivity of radio waves at the base. This reflectivity approach has been applied to several areas of Antarctica, including Dome C, Lake Vostok, Recovery Lake area, and the South Pole (e.g., Carter et al., 2009; Langley et al., 2010; Peters et al., 2005; Zirizzotti et al., 2010, 2012) and areas near ice streams, mostly in West Antarctica (e.g., Bentley et al., 1998; Jacobel, 2009). As for methodology, accurate estimation of basal reflectivity requires calibrated radar sounding data for power detection and reliable estimates of radio wave attenuation within ice by modelling of the vertical temperature field considering chemical constituents within ice (MacGregor et al., 2007). These requirements mean that any errors in any step of the estimations will introduce errors to the final estimate of the reflectivity and thus will affect the diagnosis of the bed conditions. Recently, Matsuoka et al. (2011) argued that, based on a one-dimensional ice flow model, in most cases, variations in bed returned power are dominated by variations in englacial attenuation rather than bed reflectivity. He argued that both accumulation rate and geothermal flux anomalies can interfere with the interpretation. Consequently, analytical radar algorithms that have been widely accepted are likely to yield false delineations of temperate/frozen beds. Furthermore, he argued that careful consideration is needed in diagnosing bed conditions and that, in order to improve bed diagnosis, it is necessary to simultaneously interpret the returned power and englacial reflector patterns.

In the present paper, we present analyses of radar returned power from the bed in order to determine whether bed conditions are temperate or frozen for wide area of Dronning Maud Land (DML) of East Antarctica (Fig. 1). We observe that the returned power decreases relatively simply with increasing ice thickness when the ice





TCD
6, 1781–1837, 2012



is thinner. However, the returned power is anomalously high at greater depths. Since this feature has regional characteristics, we attributed this feature to the difference in bed reflectivity. Using this feature of the data, rather than attempting to estimate the attenuation rates very accurately, we attempted to diagnose relative spatial changes in bed reflectivity (i.e., water existence at the bed) using the regional characteristics of the anomalously high returned power. Ground-based radar sounding data across DML were used for the analysis. The data are primary from a 2800-km-long traverse from the Japanese Swedish IPY 2007/2008 Antarctic Expedition (referred to hereinafter as the JASE traverse) (Holmlund and Fujita, 2009; Fujita et al., 2011) (Fig. 1) in addition to earlier ground-based radar sounding data acquired in the vicinity of Dome Fuji in 1996 and 1997 (Fujita et al., 2002, 1999). The total length of the survey route is approximately 3300 km. The survey routes include two deep ice coring sites at Dome Fuji (Watanabe et al., 1999; Motoyama et al., 2007) and at EPICA DML (Oerter et al., 2004), where the existence of water at the base of the ice sheet is known from ice coring (Motoyama, 2007; Murshed et al., 2007). The survey routes also include several reported locations of subglacial lakes detected by inspections of earlier airborne radar sounding data (Popov and Masolov, 2007). For the majority of the investigated locations, we were able to infer bed conditions. The possible error was estimated to be within several percent. Through these analyses, we determined how subglacial temperate/frozen environments are likely to be distributed in DML. We then show how they are correlated to surface elevation, ice thickness, and locations of ice divides or active ice flows. Based on analyses of subglacial environments and internal layers, we suggest a candidate area for future deep ice coring, where very old ice strata in DML can be preserved near the bottom of the ice sheet.





TCD
6, 1781–1837, 2012



## 2 Methods and study area

### 2.1 Instruments

In order to make observations deep inside the ice sheet, three radar sounders were used, as listed in Table 1. Two of the radar sounders were 179-MHz pulse-modulated radars (referred to hereinafter as 179-1 radar and 179-2 radar), and the other radar sounder was a pulse-modulated 60-MHz radar (referred to hereinafter as 60 radar). The 179-2 radar and the 60 radar were described previously (Fujita et al., 1999; Matsuoka et al., 2002). These three radars commonly use a peak power of 1 kW and three-element Yagi antennae. The 179-1 radar used a pulse of 500 ns to detect reflections from the bed of the ice sheet and a pulse of 60 ns to detect shallow (ice thickness, $H <\sim 1500$ m) internal layers. The 179-2 radar and the 60 radar used longer pulses of 1000 ns, 350 ns, and 250 ns to measure the ice thickness. The settings of the radars for the present measurement are listed in Table 2 and are discussed later herein. Different pulse widths were chosen depending on the field season (1996/1997 or 2007/2008) or on the initial scientific target of the measurements (internal layers or ice thickness). In order to measure the ice thickness of thick ice, longer pulses (1000 ns or 500 ns) were chosen. When shorter pulses were sufficient to detect ice thickness, shorter pulses (250 ns or 350 ns) were used. Data with more than two settings were also used to crosscheck ice thicknesses and to diagnosis bed conditions. The ice thickness along the JASE traverse route was reported previously by Fujita et al. (2011). Continental DEM (Bamber et al., 2009) was used to calculate surface and bed elevations along the route.

### 2.2 Factors controlling the bed returned power

In order to diagnose the conditions of ice/substrate interfaces, we investigate the behaviour of the bed returned power $[P_{\mathrm{bed}}]_{\mathrm{dB}}$ in decibels as a function of ice thickness $H$. Here, the brackets indicate numbers that are expressed in decibels. We describe





TCD
6, 1781–1837, 2012



the physical background using a radar equation. After the two-way travel of the electromagnetic waves between the radar and the ice/substrate interfaces, the bed returned power $[P_{bed}]_{dB}$ is expressed as

$$[P_{bed}]_{dB} = [S]_{dB} + [R_{bed}]_{dB} - [G_s]_{dB} - [L]_{dB} - [B]_{dB} \quad (1)$$

where $[S]_{dB}$ is the sum of the instrumental factors related to, e.g., transmission power, gains by amplifiers, cable loss, antenna gain, antenna area, and refraction loss, $[R_{bed}]_{dB}$ is the reflectivity at the bed, $[G_s]_{dB}$ is the loss of power due to geometric spreading of the electromagnetic waves along the propagation paths, $[L]_{dB}$ is the loss of power due to englacial dielectric attenuation along the propagation paths, and $[B]_{dB}$ is the loss due to birefringence effects. The term $[S]_{dB}$ is determined by the radar instruments. If the radars are stable during field use, we can take $[S]_{dB}$ as constant. The term $[R_{bed}]_{dB}$ is determined indirectly from $[P_{bed}]_{dB}$. $[R_{bed}]_{dB}$ depends on the dielectric contrasts between ice and its substrate, such as bedrock, water, or sediments. Note that, because of the much larger dielectric properties of water (e.g., Ray, 1972) compared to those of ice rock, an ice/water boundary has a by 10 to 15 dB larger Fresnel reflectivity than an ice/bedrock boundary in a simple geometric condition (e.g., Peters et al., 2005). Thus, any changes in $[R_{bed}]_{dB}$ along the survey route will be reflected as changes in $[P_{bed}]_{dB}$. The gradient of changes can be either gradual or exhibit steps/jumps in extreme cases. The roughness of the ice/substrate interfaces also affects $[R_{bed}]_{dB}$. For example, interfaces yield larger or smaller values of $[R_{bed}]_{dB}$ if the reflectors are flat (smooth) or inclined (rough). The term $[G_s]_{dB}$ is proportional to the square of the propagation length. Thus, $[G_s]_{dB}$ is $[(2H/\sqrt{\varepsilon})^2]_{dB}$ in case of the present ground-based radar sounding, where $\varepsilon$ is the dielectric permittivity of ice. The term $[L]_{dB}$ is a function of the temperature of ice, the amount of impurities within ice, and the propagation length $2H$. When the attenuation coefficient $\alpha$ dB m$^{-1}$ is a function of temperature $T$, $[L]_{dB}$ can be





TCD
6, 1781–1837, 2012



written as follows:

$$[L]_{\mathrm{dB}} = 2\int_{H}^{0} \alpha(T)\mathrm{d}z \tag{2}$$

where $z$ is the depth axis (positive downward). At radar frequencies below approximately 600 MHz, $[L]_{\mathrm{dB}}$ is practically independent of frequency in the temperature range of the polar ice sheets (Fujita et al., 2000). In addition, if the temperature field does not vary dramatically from one location to another within the ice sheet, we can expect that $[L]_{\mathrm{dB}}$ will have a smooth distribution that is approximately proportional to $H$. However, as Matsuoka et al. (2011) suggested based on the results of modelling estimation, this will not be always the case. Thus, $[L]_{\mathrm{dB}}$ is a factor that varies depending on the boundary conditions and the internal conditions. In the case of a fast ice flow above undulating bedrock topography, the dynamic conditions also fluctuate with temperature field. The term $[B]_{\mathrm{dB}}$ can appear depending on the radio frequency, the strength of birefringence in the ice, and the orientation of the antenna. The probabilities of signal extinction of returned powers of 3, 5, and 10 dB are 20 %, 12 %, and 3 %, respectively, for accidental (random) occurrence (Fujita et al., 2006). This effect can be mitigated if radar polarization is chosen properly, i.e., along ice divides, elevation contour lines, or flow lines (Fujita et al., 2006; Matsuoka et al., 2009). In such cases, the orientations of the radar polarization are close to the principal axes of the strain, where the birefringence effect is minimized. Even if the effect appears in the real data, the data will simply yield accidental (random) minima in $[B]_{\mathrm{dB}}$, which will not cause a systematic bias in $[B]_{\mathrm{dB}}$.





TCD
6, 1781–1837, 2012



Considering the nature of each of the above terms, we modify Eq. (1) using geometrically corrected bed returned power $[P^{c}_{bed}]_{dB}$, as follows:

$$[P^{c}_{bed}]_{dB} = [P_{bed}]_{dB} + [G_s]_{dB}$$
$$= [R_{bed}]_{dB} - 2\int_{H}^{0} \alpha(T)\mathrm{d}z + ([S]_{dB} - [B]_{dB}) \quad (3)$$

where the last two terms in brackets are either constant or are ignored. This equation implies that we can indirectly determine the relative variation of $[R_{bed}]_{dB}$ along the traverse route if the lateral variation of the depth-averaged attenuation is minimal. Again, note that accurate determination of $\alpha(T)$ requires reliable estimation of the depth profiles of both temperature and concentration of chemical impurities. Since the concentration of chemical impurities is determined by the deposition of aerosols, we can assume that the concentration can only change smoothly in the horizontal direction. If the lateral variation of temperature disturbs the smoothness of $\alpha(T)$ in the horizontal direction, as reported by Matsuoka et al. (2011), then the lateral variation of temperature will affect the inference of the variation of $[R_{bed}]_{dB}$ in the lateral direction. Considering this potential risk, we herein examine the lateral variation of $[P^{c}_{bed}]_{dB}$ in order to infer $[R_{bed}]_{dB}$ using real data.

### 2.3 Initial data processing

The procedures for the initial data processing were as follows. First, the data sets for the two-way travel time (TWT) from the surface to the bottom of the ice sheet were established. Then, ice thicknesses $H$ were determined based on the speed of radio waves within ice and calibration data obtained using an ice coring hole. Second, the returned peak- power from the bed $[P_{bed}]_{dB}$ in decibels was extracted. Then, the effects of geometric spreading were corrected using the value of $H$ at each site, and the geometrically corrected bed returned power $[P^{c}_{bed}]_{dB}$ in decibels was derived. Finally, data





TCD
6, 1781–1837, 2012



sets of the relationship between $H$ and $[P^{c}_{bed}]_{dB}$ were established for all of the routes. The data were averaged using a moving average over a horizontal distance of ~ 0.3 km in order to remove local fluctuations and to reduce the noise level. For the analysis of the present paper, data within 3 dB of the noise floor of the radars were rejected from the analysis of $[P_{bed}]_{dB}$ in order to avoid potential errors due to the possible non-linearity of the calibration curves near the noise floor.

### 2.4 Study area

Figure 1 shows the routes of the inland traverse at which ground-based radar sounding was performed. Most of the data are from the JASE traverse. The settings of the radars for each leg are listed in Table 1, and names and coordinates of the selected sites are listed in Table 2. For convenience with respect to the data analysis and discussion, 14 legs of a few-hundred-kilometres in length were defined, depending on the dynamic conditions of the ice sheet. These legs are labelled from A1 to F2 on the map in Fig. 1 and the cross section of the ice sheet in Fig. 2. Additional information is given in Table 3. A 150-km-long leg (A2) SSW of Dome Fuji and a 130-km long leg (A3) to the east of Dome Fuji were investigated in 1996 (Fujita et al., 1999, 2002). The distribution of the routes is characterized by several contrasting dynamic conditions of the ice sheet as explained below. For many legs, data with more than two settings were available. Such data were used to investigate the effects of different radio frequencies or different pulse widths.

(i) Vicinity of the Dome Fuji summit

Legs A1, A2, and A3 are within approximately 150 km from the Dome Fuji summit. Although these legs contain locations in the vicinity of ice divides, most of these locations are somewhat distant from the exact (within the length of the ice thickness) ice divide. An exception is the Dome Fuji summit at the centre of these three legs. Ice flows with velocities of less than approximately 2 m yr$^{-1}$ along these legs





TCD
6, 1781–1837, 2012



(Huybrechts et al., 2009; Motoyama et al., 2008; Seddik et al., 2011). Ice thickness ranges between approximately 2040 m and 3450 m.

(ii) Vicinity of the ice divide between Dome Fuji and EPICA DML core site

Legs B1, B2, and B3 are located to the south of the ice divide connecting Dome Fuji and the meeting point (MP) of the Japanese team and Swedish team in the 2007/2008 field season. These legs are located within approximately 130 km from the ice divide. Two exceptions are the Dome Fuji summit and the MP, which are located on the exact ice divide. The ice thickness ranges between approximately 1850 m and 3460 m. Leg B3 runs between the MP and NCR62, approximately 60 km from the ice divide.

(iii) Sites along the exact ice divide

Legs C1 and C2 connect Dome Fuji, the MP, and S28 almost exactly along the main ice divide of DML. These legs are characterized by very slow ice flow velocities that are well below approximately 0.2 m $yr^{-1}$ (Huybrechts et al., 2009) along the ice divide. This area is probably subject to the Raymond effect localized in the vicinity of the flow divide (Hvidberg, 1996; Raymond, 1983). The ice thickness ranges between approximately 2050 m and 3300 m. Leg C3 is an ice divide branch that originated from A28. For some reason, the radar system settings for 179-2 (500 ns) were often insufficient to detect echoes from the bed (see Fig. 2d). As a result of the insufficient information of bed echoes in this leg, we will not include this leg in the diagnosis of the bed condition in the present paper. However, prominent internal layers were detected, as shown in Fig. 2d.

(iv) Upstream of inland mountains impeding ice flow

Leg D is located between EPICA DML and Site 1 and is characterized by large changes in ice thickness from approximately 2900 m to 400 m (see Fig. 2) and slow ice flows (approximately 1 m $yr^{-1}$) (Wesche et al., 2007; Rybak et al., 2007).





TCD
6, 1781–1837, 2012



(v) Legs E1 and E2: the coastal areas of the ice sheet

Leg E1 is located near the coast of the ice sheet in Western DML. The leg connects an area of Heimefrontfjella (Heimefront Range) and the Swedish Wasa Station. Leg E2 is located near the coast of the ice sheet in Eastern DML. These legs connect S16, Mizuho, and MD170. These legs are also characterized by large changes in ice thickness (from approximately 2500 m to < 100 m) and surface elevation (from approximately 2800 m to 200 m). In addition, there are local areas in which the ice flow velocity is high compared to the surroundings (Motoyama et al., 1995; Näslund et al., 2000). An apparent ice stream is known to exist at the Veststraumen ice stream, near the Swedish Svea Station (Fig. 1) (Näslund et al., 2000).

(vi) Legs F1 and F2: mid-stream area

Legs F1 and F2 are characterized by large fluctuations in ice thickness (Fig. 2, with an amplitude of approximately 1000 m and a periodicity of approximately 20 km) and relatively high ice flow velocities of up to approximately 18 m $yr^{-1}$ (Motoyama et al., 1995). These conditions are quite different from the other legs in the polar plateau, for which the ice flow velocity is well below a few meters per year (Huybrechts et al., 2009).

In addition to the distribution of ice thickness, we present one of the isochrones (englacial radar reflectors) that was detected by radar in Fig. 2. The reflector appeared continuously along almost all of the radar profiles across DML. The depth at the Dome Fuji ice coring site is 1171 (±10) m, which is dated to be 73.3 (±4) kyr BP based on the dating of the Dome Fuji ice core (Parrenin et al., 2007). Using the 179-2 radar, we also identified that the same layer is located at a depth of 1882 (±10) m at EPICA DML. The depth is dated to be 73.6 (±4) kyr BP based on the dating of the EPICA DML ice core (Ruth et al., 2007). This englacial reflection layer is likely caused by the Toba supereruption that occurred sometime between 69 ka and 77 ka ago at Lake Toba (Sumatra, Indonesia) (Chesner et al., 1991; Ninkovich et al., 1978).





TCD
6, 1781–1837, 2012



## 3 Results

### 3.1 Vicinity of the Dome Fuji summit

Figure 3a, c show the relationships between $[P^{c}_{bed}]_{dB}$ and $H$ along the "A" legs. We hereinafter refer to this type of graph as a H-P plot. The results for two different frequencies are shown in Fig. 3a, c. The distribution of the data reveals that $[P^{c}_{bed}]_{dB}$ tends to decrease with increasing $H$. At $H$ greater than approximately 2800 m, $[P^{c}_{bed}]_{dB}$ tends to increase or to become independent of ice thickness, despite increasing $H$. Here, we discuss only signals that are well above the noise floor. Thus, the features of the data here are not caused by the noise floor, as indicated by blue lines in the graphs of Fig. 3a, c. Figure 3b, d show the spatial distributions of $H$ and $[P^{c}_{bed}]_{dB}$ with respect to horizontal distance $x$ for two different frequencies. We hereinafter refer to this type of graph as an X-PH plot. An important feature of Fig. 3b, d is that we adjusted the scales of the left-hand and right-hand axes using the gradient of a regression line found in the region of thinner ice ($<\sim 2800$ m) of the H-P plot, as indicated by the red lines in Fig. 3a, c. The range of $H$ for the regression line was determined such that the analysis is virtually unaffected by the values of $[P^{c}_{bed}]_{dB}$, which increased near $H$ of approximately 2,800 m. For this purpose, the range of $H$ was chosen to be between approximately 2000 m and 2600 m. This method of scaling in X-PH plots highlighted locations at which $[P^{c}_{bed}]_{dB}$ increases with increasing $H$ in the region of thicker ice ($>\sim 2800$ m), which enables us to examine the characteristics of the data in a point-by-point manner. We find that the data for the two different frequencies are very similar in Fig. 3b, d, even with respect to some of the minute details of the fluctuations. In order to determine whether there are systematic frequency dependences, a scatter plot of $[P^{c}_{bed}]_{dB}$ (60 MHz, 250 ns) versus $[P^{c}_{bed}]_{dB}$ (179 MHz, 350 ns) is presented in Fig. 4a. All of the data points in Fig. 3 are plotted in Fig. 4a. The data distribution is found to be linear and the data are scattered from the linear trend by a few dB at most. In other words, as shown in the panels, the distribution having increases at large $H$ is fairly common at two different radio frequencies. As an observational fact, the variations of the





TCD
6, 1781–1837, 2012



$[P^{c}_{bed}]_{dB}$ are independent of the choice of radio frequency. This supports the argument that the effect of birefringence $[B]_{dB}$ is negligible along the series A legs. In addition, at each of the two frequencies, 60 MHz and 179 MHz, the variations (the increase for $H$ larger than approximately 2800 m) of $[P^{c}_{bed}]_{dB}$ are independent of the radar pulse width. Two examples are shown in Fig. 4b, c. Figure 4b is a scatter plot of $[P^{c}_{bed}]_{dB}$ (60 MHz, 1000 ns) versus $[P^{c}_{bed}]_{dB}$ (60 MHz, 250 ns) for leg A3, and Fig. 4c is a scatter plot of $[P^{c}_{bed}]_{dB}$ (179 MHz, 350 ns) versus $[P^{c}_{bed}]_{dB}$ (179 MHz, 250 ns) for leg A1. Once again, the data distribution is fairly linear, and the data are scattered from the linear trend by a few dB at most. Therefore, the increase that occurs for $H$ larger than approximately 2800 m is also independent of the choice of radar pulse width.

Remarkably large $[P^{c}_{bed}]_{dB}$ values are found in the approximate range of $x$ = 850 km to 1000 km and at $x$ greater than 1120 km in Fig. 3b, d. The deviation from the regression line sometimes exceeds approximately 20 dB in the scale of the $[P^{c}_{bed}]_{dB}$. Another example of remarkably large $[P^{c}_{bed}]_{dB}$ is the location indicated as East 95. Note that a location in the vicinity of the site East 95 was reported by Popov and Masolov (2007) as a site of a subglacial lake (Lake ID 97 in their paper) detected using their airborne radar sounding data. This location is shown on the map in Fig. 11.

### 3.2 Vicinity of the ice divide

Figure 5a is a H-P plot along the series B legs. Again, two different frequencies were used. Since we also confirmed the linearity and similarity between the data for the different frequencies, we will present the data for only one of the frequencies throughout the remainder of the present paper. The distribution of the data again exhibits an increase in $[P^{c}_{bed}]_{dB}$ at large $H$. Compared with Fig. 3a, there are fewer data points for smaller $H$ and more data points for larger $H$. Figure 5b is the X-PH plot along the same legs. Again, the regression line in the H-P plot (Fig. 5a) shows the left-hand and right-hand scales of the X-PH plot. The range of $H$ for the regression analysis was again less than 2600 m. In Fig. 5a, remarkably high peaks of $[P^{c}_{bed}]_{dB}$ were observed





TCD
6, 1781–1837, 2012



at $H = \sim 3300$ m. In Fig. 5b, these peaks occur over an area approximately 25 km wide near RT411 (see Table 2 for the exact location). Again, this location was reported by Popov and Masolov (2007) as the site of a subglacial lake (Lake ID 89 in their paper. See Fig. 11 of the present paper). As shown in Fig. 5b, the profiles of $[P^{c}_{bed}]_{dB}$ exhibit large deviations from the profiles of $H$ when $H$ is large. Remarkable examples are found in the approximate ranges of $x = 190$ km to 350 km and 410 km to DF, and along leg E3 from the MP to NCR62. The deviation from the regression line sometimes exceeds approximately 20 dB in the scale of $[P^{c}_{bed}]_{dB}$. Site RT313 and NCR62 are the locations of subglacial lakes, which were reported by Popov and Masolov (2007) as Lake ID 93 and Lake ID 91.

### 3.3 Sites along the exact ice divide

Figure 5c shows a H-P plot along legs C1 and C2. The distribution of the data is markedly different from the distribution in the series A and B neighbouring legs. One of the difference is that, for given values of $H$, the data points tend to have $[P^{c}_{bed}]_{dB}$ values that are higher than those of the neighbouring legs by approximately 10 to 15 dB. In addition, we do not find any inflection, i.e., sudden increase at $H = 2800$ m. Moreover, for given values of $H$, the variability of $[P^{c}_{bed}]_{dB}$ is greater than in the neighbouring legs. In contrast, at $H > \sim 2800$ m, values of $[P^{c}_{bed}]_{dB}$ are as high as in the data for the series A and B neighbouring legs. Considering all of these features, we assume that the major source of the difference between legs C1 and C2 and the neighbouring legs is $[R_{bed}]_{dB}$ and not the conditions of the attenuation term in Eq. (3). If the major cause is the attenuation term, the influence should also appear in the $[P^{c}_{bed}]_{dB}$ values for $H > \sim 2800$ m. Therefore, we assume that the $[R_{bed}]_{dB}$ values for $H < \sim 2800$ m are not the same as those in the neighbouring legs. Based on this assumption, we use the regression line of the series B legs to make the X-PH plot for legs C1 and C2 comparable with the X-PH plot for the neighbouring legs. We will discuss the meaning of the data features in the discussion section later herein.





TCD
6, 1781–1837, 2012



### 3.4 Upstream of inland mountains

Figure 6a, b shows the H-P and X-PH plots along leg D. The results from radar 179-2 obtained using a 1000-ns pulse are shown. The distribution shown in Fig. 6a increases at a $H$ of approximately 2600 m. In order to extract the distribution of the data well above the increase depth, we explored the range of $H$ for the regression line and found that the range of $H$ = 1500 to 2500 m is virtually unaffected by the increase and represents well the data distribution. Using the regression line, we scaled the axes of the X-PH plot in Fig. 6b. The profiles of $[P^{c}_{bed}]_{dB}$ and $H$ agree well at $x$ locations of smaller $H$. However, the $[P^{c}_{bed}]_{dB}$ values deviate from the regression line by 10 to 15 dB at $x$ locations at which $H$ is greater than approximately 2500 m as well as above a few subglacial mountains in the range of $x$ = 2350 m to 2450 m. The EPICA DML site is located in such a region, in which the $[P^{c}_{bed}]_{dB}$ values deviated by approximately 15 dB from the regression line.

### 3.5 Coastal area

Figure 6c, e shows the H-P plots along legs E1 and E2, respectively. In these figures, the distribution increases at $H$ of approximately 1000 m and approximately 1500 m, respectively. The regression lines were again investigated in order to ensure that the gradient was virtually unaffected by the increases and represents the data distributions for smaller $H$. The ranges for the regression lines were chosen as the red lines in Fig. 6c, e. Figure 6d, f show the X-PH plots for these regression lines, which clearly indicate the $x$ locations at which the profiles of $[P^{c}_{bed}]_{dB}$ and $H$ agree or disagree. In leg E1, disagreement occurred at locations at which the traverse route crossed the Vestraumen ice stream (Näslund et al., 2000) (2625 km < $x$ < 2725 km) and another ice stream at $x$ =~ 2560 km. In leg E2, on the marginal side of the ice sheet ($x$ < 100 km), the profiles of $[P^{c}_{bed}]_{dB}$ and $H$ agree. However, these profiles disagree at some locations (100 km < $x$ < 160 km and $x$ > 190 km), where the ice flow velocities are known to be faster (see the flow velocities in Fig. 6f). Geographically, this area is located





TCD
6, 1781–1837, 2012



directly upstream of the Soya Coast, where Sawagaki and Hirakawa (1997, 2002) observed a landform of bedrock that appears to have been eroded by subglacial melt water sometime in the past. For $x >\sim 250$ km, we observed no features indicating synchronization between the variations of $[P^{c}_{bed}]_{dB}$ and $H$. This area is located upstream of the Shirase Glacier (Fig. 1), where most of the ice flows across this drainage basin (drainage basins are delineated by thin blue lines in Fig. 1) to the sea.

### 3.6 Mid-stream areas

Figure 7a, c shows the H-P plots of legs F1 and F2, respectively. For these legs, we can find neither a clear decrease in $[P^{c}_{bed}]_{dB}$ with increasing $H$ nor a clear increase in $[P^{c}_{bed}]_{dB}$ at large $H$. As for leg F1, Fig. 7a shows a distribution of data that is similar to the distributions in the series A neighbouring legs in Fig. 3. In other words, there is a slope at $H <\sim 2400$ m. At $H >\sim 2400$ m, $[P^{c}_{bed}]_{dB}$ fluctuates or increases slightly with increasing $H$. As for leg F2, Fig. 7c shows the fluctuation of $[P^{c}_{bed}]_{dB}$ with respect to $H$ with slightly increased $[P^{c}_{bed}]_{dB}$ on the left. The amplitude of fluctuation in $[P^{c}_{bed}]_{dB}$ is approximately 15 dB, which is greater than that in leg F1, which is approximately 10 dB.

Along leg F1, the X-PH plot is given in Fig. 7b using the regression line determined in Fig. 7a, so that the gradient is as large as that for the series A neighbouring legs. In Fig. 7b, agreement is found at the most inland part at $x >\sim 820$ km. At $x <\sim 820$ km, good correlation is not found between the fluctuations of $H$ and $[P^{c}_{bed}]_{dB}$. Within the given scale of the axes, $[P^{c}_{bed}]_{dB}$ fluctuates more than $H$. This feature is similar to that observed for the series A neighbouring legs (Fig. 3).

As for leg F2, it is not possible to identify ranges of $H$ that are suitable for producing a linear regression line. However, we attempted to produce an X-PH plot in order to compare the fluctuations of $H$ and $[P^{c}_{bed}]_{dB}$ with respect to $x$. Figure 7d shows the X-PH plot for leg F2. We simply adjusted the scales of the left and right axes using the same gradient as in leg F1. Along the leg, fluctuations of both $H$ and $[P^{c}_{bed}]_{dB}$ are similar in scale, approximately 10 to 20 km. However, within the given scale of the axes,





TCD
6, 1781–1837, 2012



the fluctuation of $[P^c_{bed}]_{dB}$ is greater than that of $H$. Small scale features do not agree between the fluctuations of $H$ and $[P^c_{bed}]_{dB}$ along leg F2. $[P^c_{bed}]_{dB}$ fluctuates by 10 to 20 dB. Sharp peaks of $[P^c_{bed}]_{dB}$ with widths of approximately 1 km to several kilometres often appear at locations of subglacial mountains.

### 3.7 Results summary

In summary, the general data properties are as follows.

(i) The H-P plots show that $[P^c_{bed}]_{dB}$ decreases as the ice becomes thicker. This trend is observed only when the ice is thinner than a certain value, $H_0$, which ranges between 2600 m and 2800 m in the inland region (series A, B, and C legs) and is approximately 2400 to 2500 m in the midstream areas (series D and F legs) and approximately 1000 to 1500 m in the coastal area (series E legs).

(ii) In these areas, $[P^c_{bed}]_{dB}$ has a different depth dependence at depths greater than $H_0$. If the depth dependence in the shallower ice continues beyond $H_0$, it is very likely that the bed will not be detected by the radars used in the present study.

(iii) We analyze these features only if the bed returned power is 3 dB greater than the noise level in the geometrically corrected returned power, which increases slightly with ice thickness. Therefore, the observed data features are robust.

(iv) These features are nearly independent of the radar frequency and radar pulse width.

(v) In the mid-stream areas, it was difficult to find clear features of (i) and (ii).

(vi) We linearly approximate the depth variation of $[P^c_{bed}]_{dB}$ at depths of less than $H_0$. The gradient of this linear approximation is used to scale the relationship between ice thickness and returned power in the X-PH plots.





TCD
6, 1781–1837, 2012



(vii) The gradient can be different if data for a different depth range are used for the approximation. However, the ambiguity of the analysis does not change the regional pattern of the X-PH plot.

(viii) A large difference between the measured $[P^{c}_{bed}]_{dB}$ and the value predicted by extrapolation of the linear approximation above is found over continuous distances of more than 100 to 200 km in most areas, which indicates that this feature is related more to the regional glaciological conditions.

## 4 Discussion

### 4.1 Empirical methods to diagnose bed conditions

Based on the observations described in Sect. 3, we assess the subglacial environments along the radar profiles. Concretely, we attempt to identify both temperate and frozen beds by analyzing various features of $[P^{c}_{bed}]_{dB}$ fluctuations as functions of $H$ and $x$. In the following, we discuss the types of behaviours expected for the radar returned power and basal reflectivity in order to develop analytical procedures for assessing bed conditions (temperate or frozen). Although more complicated situations can occur, the goal is to develop an analytical method for distinct cases.

When the depth-averaged attenuation rate is uniform over a surveyed leg, the total attenuation associated with the reflection from the bed is proportional to the ice thickness $H$. When the bed reflectivity is also approximately uniform (either temperate or frozen), the geometrically corrected returned power $[P^{c}_{bed}]_{dB}$ decreases linearly with ice thickness $H$. Continental ice-flow modelling predicts that the base of the ice sheet is melting in the majority of the inland area (Pattyn, 2010). Smaller surface accumulation and thicker inland ice cause the effects of cold-ice advection from the surface to be less significant than those in the coastal area. Although the geothermal flux remains largely unknown in Antarctica, ensemble experiments reveal that the above view is consistent, regardless of the uncertainty in the geothermal flux.





TCD
6, 1781–1837, 2012



Radar data from the inland area (series A and B legs) reveal that the linear decrease in $[P^{c}_{bed}]_{dB}$ appears only to a certain ice thickness $H_0$. We derived the least-squares-fit slope of this portion of the data. If bed reflectivity is uniform, half of this slope gives the one-way depth-averaged attenuation rate $< N >$ (Table 4). For series A legs, $< N >$ can be calculated as 12 dB km$^{-1}$ when the ice thickness ranges between 2050 m and 2600 m. Provided that $< N >$ is uniform regardless of the ice thickness over the series A legs, the expected bed returned power is −45 dB when the ice is 3200 m thick (see Fig. 3a). When the ice is 800 m thicker, from 2600 m to 3200 m, with all other factors remaining unchanged, the depth-averaged attenuation rate can be larger, but only slightly (Matsuoka et al., 2011). For instance, when $< N >$ differs by 2 dB km$^{-1}$ one way, an 800-m increase in the ice thickness gives a 3.2 dB larger attenuation, which cannot explain the observed bed returned power. Therefore, we believe that the larger bed returned power at greater depths are caused primarily by the larger bed reflectivity, rather than regional variations in other factors. The bed reflectivity can change with the bed roughness in the scale of radio-wave wavelengths and the substance at the base. Although the effect of the bed roughness is radar-frequency dependent, our data show that the features mentioned above are in essence radar-frequency independent. Therefore, we argue that the larger bed returned power from greater depths is caused by the presence of water, rather than variations in englacial attenuation or bed roughness.

Depth-averaged attenuation rates derived from the slope of the H-P plot depend weakly on the range of the ice thickness. We examined the sensitivity of the bed diagnosis in terms of the choice of the depth range for attenuation-rate estimates and found that the regional pattern of the temperate/frozen beds remains unchanged regardless of the choice of the thickness range.

Based on the behaviours expected for the radar returned power and basal reflectivity, we propose the analytical procedure shown in Fig. 8 for assessing bed conditions. The basic steps are as follows, and the details are provided in Fig. 8. Step 1: preliminary observation of the data using the H-P plot. Step 2: check whether the gradient of the





TCD
6, 1781–1837, 2012



regression lines are explicable by dielectric attenuation within ice. Step 3: diagnose the temperate and frozen conditions using the X-PH plot point by point for each location $x$. Step 4: if ambiguity remains or further information is necessary, we perform cross checks and collect more information of circumstantial evidence. Step 5: check for the features caused by possible sources of errors. We check from one leg to another how well the proposed procedure works.

## 4.2 Diagnosis of the subglacial environment

### 4.2.1 Vicinity of Dome Fuji summit

As described in Sect. 3.1, these legs were characterized by a linear decrease in $[P_{\mathrm{bed}}^{\mathrm{c}}]_{\mathrm{dB}}$ with increasing $H$ in the range of $H <\sim 2800$ m. The gradient of the linear distribution was reasonably explained by the attenuation coefficient within ice, as shown in Table 4. Based on these conditions, we distinguished between a temperate bed and a frozen bed using the X-PH plot of Fig. 3b, d. We diagnosed point by point whether the data point belongs within a shallower linear distribution or to deviated points that are often found at deeper depths. The results of the diagnosis are shown in a few different types of data plot. In Fig. 9a, the results of the diagnosis are shown in the H-P plot by blue dots for the frozen bed and red dots for the temperate bed. On the cross-sectional map of the ice sheet in Fig. 10 and the bed topography map of DML in Fig. 11, we expressed the bed conditions using the blue and red dots again. Note that the series A legs were investigated by several different radar settings, as listed in Table 1. These different settings yielded consistent diagnosis results. As for the error probability, we estimate that the error could occur only near the temperate/frozen boundaries. We estimate the error rate at approximately 3 %. The statistics for the diagnosis results are listed in Table 5.

The results of the diagnosis for the series A legs suggest that these legs are characterized by a mixture of temperate and frozen beds, depending primarily on the values of $H$. The diagnosis results are in agreement with the reported distribution of subglacial





TCD
6, 1781–1837, 2012



lakes and bed conditions of the deep ice coring hole. Data suggest that the bed is saturated with liquid water in wide zones when $H > \sim 2800$ m. There are frozen conditions only when $H < \sim 2800$ m in this area. At some locations above subglacial mountains, the bed is temperate, even if $H$ is as small as approximately 2400 m. We believe that this temperate bed in shallow conditions occurred due to a special ice flow condition at ice divides known as the Raymond effect (Hvidberg, 1996; Raymond, 1983). Our interpretation of this phenomenon is as follows. The deformation in ice in the vicinity of ice divides is different from that in the vicinity of sheet flow. In the ice-divide zone, the surface slope drops to zero and the flow solution changes. The longitudinal strain rate is high, especially in the upper layers, and the vertical velocity is smaller than away from the divide. The horizontal shear strain increases gradually down to the bed and is less concentrated at the centre of the ice divide in comparison to the flanks. The vertical velocity smaller than away from the divide make advection of cold ice mass from the surface smaller. Then, at some locations directly above subglacial mountains, the thermal-insulation effect of the ice sheet appears more strongly than in flank areas, in which the vertical flow velocity is larger. The ice/bed interface can then reach the pressure melting point due to the accumulation of geothermal heat flux. Therefore, the basal temperature appears to depend on how each site is affected by the Raymond effect. The Raymond effect will be discussed further for the series B and C legs because ice divides are included in these legs. Note that the Raymond effect makes the bed temperate at the melting point but will not affect the temperature gradient within ice strongly. This is because, in any case, the bed temperature can never be higher than the pressure melting point. Geothermal heat flux will be consumed by the heat of fusion, and the Raymond effect should appear primarily in the melting rate at the base.

#### 4.2.2 Vicinity of the ice divide

The diagnosis procedure and the presentation methods are the same as in the series A legs (see Figs. 9b, 10, and 11 and Table 5). The series B legs are the neighbouring and continuous legs of series A. Thus, the diagnosed results should be similar.





TCD
6, 1781–1837, 2012



Compared to the series A legs, the series B legs have a greater proportion of temperate bed because $H$ tends to be large. According to Fig. 5b, an approximately 300-km zone from DF to RT188 is nearly saturated with basal water. Both DF and RT411 (Lake ID 89 in Popov and Masolov, 2007) are located in a common and connected subglacial water environment. Near MP, where $H$ ranges between approximately 2800 m and 2400 m, the bed was diagnosed as temperate, although $H$ is small. We believe that this temperate bed at the ice divide is due to the Raymond effect.

#### 4.2.3 Sites along the exact ice divide

For the diagnosis of the series C legs, Step 4 in the diagnosis procedure was necessary. In other words, the regression analysis for the frozen part of the bed could not be performed using the data within C1 and C2 alone. Diagnosis could be performed only by comparing the data with the series A and B neighbouring legs. The entirety of legs C1 and C2 should be under the Raymond effect. We diagnosed almost all points as temperate (see Figs. 9c, 10, and 11 and Table 5). The features of the data described in Sect. 3.3 are explicable by the existence of water, even when $H$ is as small as approximately 2200 m. The data are explicable only by systematically high reflectivity at the bed.

#### 4.2.4 Upstream of the inland mountains

Based on the standard procedures described in Fig. 8, we distinguished between the temperate bed and the frozen bed using the X-PH plot of Fig. 6b in a point-by-point manner. We diagnosed the bed condition, as shown in Figs. 9d, 10, and 11 and Table 5. The bed of the EPICA DML ice coring site (2774-m-thick ice) was diagnosed to be well within the temperate condition (see Fig. 9d). This is in agreement with earlier drilling experience indicating that melted water was detected at the borehole (Murshed et al., 2007). When we move from the EPICA DML to the direction of Heimefrontfjella (Fig. 1), the bed is temperate at some subglacial trough locations. Exceptionally high





TCD
6, 1781–1837, 2012



$[P^c_{bed}]_{dB}$ values are found at locations at which $H$ is as small as approximately 1500 m. This situation is clarified by the dynamic condition of leg D, which is characterized by transition from the ice divide near EPICA DML to the area influence by the damming effect of the subglacial mountains near Heimefrontfjella. As a result of the damming effect, the vertical component of the ice flow is generally small, which is similar to the condition at the ice-divide flow (e.g., Nishio and Mae, 1979; Cuffey et al., 2010). Thus, geothermal heat is more easily accumulated at the bed.

#### 4.2.5 Coastal regions

In legs E1 and E2, based on the standard procedures, we diagnosed the bed condition as shown in Figs. 9e, 10, and 11 and Table 5. In contrast to the situations of the inland plateau, $H$ ranges down to approximately 400 m. In this thinner ice near the coast of the ice sheet, the majority of the bed is frozen, except at locations of active ice flow in subglacial troughs. In leg E1, temperate bed is identified at locations where the route crosses a few ice streams. One such location is the Veststraumen ice stream. This also agrees with the location of an outlet glacier from Heimefrontfjella (figure not shown). In leg E2, we predicted that the bed at $x > 100$ km is temperate. Figure 6e, f suggest a very large increase in $[P^c_{bed}]_{dB}$ as we move inland from the coast, particularly at locations near Mizuho. The characteristics of the data in the H-P plot (Fig. 6f) are very similar to those of legs containing subglacial lakes (Figs. 3a and 5a). We hypothesize that subglacial water flow is active near Mizuho, where active ice flow and thinning of the ice-sheet has been observed (Mae and Naruse, 1978; Motoyama et al., 1995). Considering the ice sheet topography and the bed topography, as shown in Fig. 11, the subglacial water is flowing toward the Shirase Glacier. The area near Mizuho and MD12 constitute a trough zone. Subglacial water from a zone on the Southeast side can only drain toward Shirase Glacier through an area in the vicinity of Mizuho and MD12. Further inland, between Mizuho and MD170, the bed was diagnosed as entirely temperate based on a number of features. (i) In the H-P plot (Fig. 6e) there are no features indicating basal freezing. In addition, $[P^c_{bed}]_{dB}$ and $H$ do not show any particular





TCD
6, 1781–1837, 2012



correlation. This indicates that bed conditions dominate the fluctuation of $[P^{c}_{bed}]_{dB}$. (ii) The leg has larger $H$ than the area near Mizuho, where the bed is diagnosed to be temperate. The larger $H$ suggests that the bed in this area cannot be colder than the neighbouring area near Mizuho.

#### 4.2.6 Mid-stream areas

Legs F1 and F2 are characterized by little features of decrease in $[P^{c}_{bed}]_{dB}$ with increasing $H$. Thus, it is not possible to diagnose the bed conditions using the procedures used for the other legs. We need to examine these legs primarily by Step 4 in Fig. 8, i.e., by the collection of additional information. First, leg F1 is next to leg A1, where the bed is temperate in the majority of the leg. The H-P plot shown in Fig. 7a has characteristics indicating a decrease in $[P^{c}_{bed}]_{dB}$ with increasing $H$ at depths shallower than approximately 2400 m. We apply the gradient of neighbouring leg A1 to the shallow portion of leg F1. As shown in Fig. 7b, the bed of leg F1 is generally temperate. In Fig. 7a, b, no clear correlations between $[P^{c}_{bed}]_{dB}$ and $H$ appear when $H$ is more than approximately 2500 m, implying that the $[R_{bed}]_{dB}$ has a high variability of approximately 15 dB in spatial distribution. This situation is explicable by the heterogeneous distribution of basal water.

In leg F2, it is not possible to specify any features indicating boundaries between temperate/frozen conditions. Fluctuating dynamic/thermal fields appear to affect $[P^{c}_{bed}]_{dB}$. There are some examples of modelling the ice flow of this area, including the temperature field (Pattyn and Decleir, 1995; Saito and Abe-Ouchi, 2004). Although these studies used a smooth bed topography for modelling, the temperature field fluctuates when the bed topography undulates. A problem in diagnosing the bed is the large gradient of the attenuation term in Eq. (3). In addition, the attenuation term should fluctuate highly. Moreover, the accumulation rate in this zone also fluctuates highly due to the undulating surface slope. This appears to be the most difficult region for diagnosis based on the temperature field (e.g., Matsuoka et al., 2011). The conditions of leg F2 are as follows:





TCD
6, 1781–1837, 2012



(i) Neighbouring legs E2 and F1 are almost entirely temperate. Thus, temperate bed conditions are most likely dominant.

(ii) In neighbouring legs E2 and F1, locations with $H$ greater than approximately 1500 m and greater than approximately 2400 m, respectively, are temperate. Therefore, in leg F1, the temperate/frozen boundary $H$ ranges most probably between 1500 m and 2400 m. Based on a conservative estimation, we believe that locations with $H > 2400$ m are temperate. In this leg, approximately 60 % of locations have $H > 2400$ m. In the remaining approximately 40 % locations, $H$ ranges between 1780 m and 2400 m. For these locations, we are not able to delineate a clear boundary separating temperate bed from frozen bed. At some locations, the bed may remain frozen.

(iii) The surface slope in leg F2 is 0.25° to 0.30° steeper than the surface slope in leg F1, which ranges from 0.10° to 0.25° (e.g., Fujita et al., 2002). In addition, the flow speed in this leg ranges from 4 to 17 m yr$^{-1}$ (Motoyama et al., 1995). These conditions imply that the driving force for the ice flow is much stronger than in leg F1. Then, internal deformation and/or basal slippage are conditions favourable to heat production and thus make the bed temperate.

(iv) Many of the observed features appear to suggest that the entire leg is temperate at the bed. In particular, sharp peaks in $[P^{c}_{bed}]_{dB}$ with widths of approximately 1 km to several kilometres often appear at locations of subglacial mountains. This appears to suggest that the bed is temperate even at the peaks of subglacial mountains. Although many features are favourable for basal melting, it is not possible to conclusively diagnose the remaining approximately 40 % of locations. Like the other legs, the results of diagnosis are presented in Figs. 9, 10, and 11 and Table 5.





TCD
6, 1781–1837, 2012



### 4.3 Spatial distribution of the subglacial environments

The distances of the temperate bed and frozen bed along the legs investigated in the present paper are listed in Table 5. We estimated that 62 % of the surveyed profile has a temperate bed, while 23 % has a frozen bed. The proposed method cannot diagnose the bed condition for 15 % of the surveyed profile. We estimate that the uncertainty of these values is roughly several percent, based on uncertainty in order to determine the boundaries between temperate bed and frozen bed. We did not include leg C3. The fraction of the temperate bed to the dry bed estimated here is similar to that predicted by the ice-flow model (55 % temperate, 45 % cold) (Pattyn, 2010). The discrepancy between these estimates is partly due to the fact that the radar data do not equally sample the region. Nevertheless, the present analysis provides a useful validation measure of ice-flow models. The observation and the model-based estimation of the present study appear to agree. We believe that the numerical modelling should be based on the diagnosis results of the present study in order to improve the estimates of geothermal heat flux. Moreover, note that actual zones for melt water production are far wider than known local areas of subglacial lakes. The existence of the lakes indicates the existence of topographic troughs that are capable of preserving water within the vast zone of water production at the temperature of the pressure melting point.

Figure 12a, b show the subglacial conditions in the plot of $H$ (ordinate) versus surface elevation (abscissa) for the legs in the Shirase Glacier drainage basin, including the Dome Fuji area, and for the legs between Wasa and Dome Fuji, respectively. Again, the colours of the trace represent the subglacial conditions. The purpose of this plot was to visualize how the temperate/frozen boundaries are distributed as a function of surface elevation and $H$. One important feature is that lower surface elevation and thicker ice are favourable conditions for the temperate bed. Qualitatively, this is explainable by the advection of cold ice from the ice sheet surface and the geothermal heat flux from the bottom of the ice sheet. An ice sheet can act as a more efficient insulator when the ice is thicker. This has a very important effect on the dynamics of the ice sheet. (i) In DML,





TCD
6, 1781–1837, 2012



the bed inland of the ice sheet tends to be temperate. Frozen areas of subglacial high mountains where ice thickness is less than approximately 2800 m are an exception. (ii) In contrast, the bed of the coastal areas tends to be frozen. Areas of fast-flowing ice of subglacial lowland or troughs are an exception. These observations suggest a general picture of the ice sheet in DML in which subglacial water is dominantly produced at the bed of the wide inland plateau and that the water is discharged to the sea primarily through the bed of fast-flowing ice. Figure 12a, b demonstrate that conditions (i) and (ii) are common in two contrasting dynamic conditions.

It has been suggested that as much as 90 % of the discharge from the Antarctic ice sheet drains through a small number of fast-moving ice streams and outlet glaciers fed by catchment areas. Previous studies have shown that the major ice stream systems have complex systems of tributaries that extend far inland (e.g., Bamber et al., 2006, 2000; Bennett, 2011; Pattyn et al., 2005; Rignot et al., 2011). Rignot et al. (2011) demonstrated that ice stream systems with complex systems of tributaries are controlled by the variations of the slipperiness of the substrate. Based on our observation of the ice sheet bed, we suggest that the distribution of the temperature of bed conditions (i) and (ii) are closely associated with both the slipperiness of the substrate and the distributions of ice stream systems with complex systems of tributaries that extend far inland.

### 4.4 Implications for age of very deep ice in DML and other regions of Antarctica

Our analysis revealed that both Dome Fuji and EPICA DML ice core sites have temperate beds, which is consistent with the borehole observations (Motoyama, 2007; Murshed et al., 2007). The age of the deepest ice with basal melting remains younger than that in areas in which basal melting does not occur, provided that everything else is kept equal. Drilling into the million-years-old ice is highly prioritized by IPICS (Wolff et al., 2006; Jouzel and Masson-Delmotte, 2010). Here, we discuss candidate sites of the drilling to the million-old ice. The relative depths of the 73.3 (±4) kyr prominent time marker to the local ice thickness is largest in the vicinity of Dome Fuji, implying that





TCD
6, 1781–1837, 2012



very old ice might be preserved in the ice sheet near Dome Fuji. Near MD12 and near EPICA DML, the 73.3 (±4) kyr layer is very close to the ice sheet bed, which appears to be associated with active subglacial melting and active ice flow. In areas surrounding Dome Fuji, at locations at which the surface elevation is lower than 3700 m, the subglacial condition is mostly temperate (Fig. 11). Therefore, ice older than the oldest age of the Dome Fuji ice core (~ 720 kyr BP at a depth of 3035 m) (Motoyama, 2007; Motoyama et al., 2007) is not expected to remain near the bottom of the ice sheet. Therefore, the vicinity of the Dome Fuji summit (surface elevation > 3700 m) appears to be the only candidate for finding ice older than ~ 720 kyr. Recent studies of ice sheet modelling (Pattyn, 2010; Seddik et al., 2011) commonly indicate that older ice strata are preserved above the mountainous area with frozen bed near the dome as highly compressed strata in the vertical direction. Based on the radar diagnosis in the present study, we believe that the subglacial frozen zone in the vicinity of Dome Fuji is a candidate area for the oldest ice strata obtainable in DML.

We examined data for radio wave internal reflections and the distribution of isochrones (englacial radar reflectors) near Dome Fuji. A candidate area for future ice coring was found. Fig. 13 shows a cross-section of the ice sheet along legs A1 and A2 near Dome Fuji. The figure shows the surface elevation, the elevation of several dated isochrones and isochrones of unknown age, and the bed elevation with the diagnosed subglacial conditions. Scattering of radio waves from within ice is presented in grey scale ranging between −105 and −115 dBm in order to show very deep strata. There are subglacial mountains SSW of DF (Fig. 10 and 11). The ice/bed interface at the mountains is diagnosed as frozen. Above the mountains, radio wave scattering was observed from very deep ice, which has the shape of a dome having a width of approximately 20 km at a site SSW47 (Fig. 13). In both sides of the dome-shaped ice, internal layers drop steeply toward the temperate bed. This image implies that ice of the same age exists at depths much closer to the bed, which is presumably caused by the local alternations of wet and dry beds. Another interesting feature is that when we move SSW from SSW47, the same scattering zone appears with a higher scattering





TCD
6, 1781–1837, 2012



strength (Fig. 13). Fujita et al. (1999) suggested that the increase in the scattering strength at this location is due to the contrast of crystal orientation fabrics caused by high shearing between the ice flow and the bed. Thus, the shearing zone near SSW90 (Fig. 13) is less preferable for ice coring for the purpose of the paleoclimatic studies. The ice dome zone at SSW47 is the preferable site. The dome-shaped ice can contain very old ice, although we are unable to date this ice. The area near SSW47 should be investigated for future ice coring.

Comparison of the DF area and the Dome A and Dome C areas shows regional characteristics of subglacial conditions near the dome summits in East Antarctica. Bell et al. (2011) found that in the vicinity of Dome A the base of the ice sheet has refrozen ice in the 24 % of the surveyed area. The freeze-on results from conductive cooling of water that pounded near the Gamburtsev Subglacial Mountain ridges and the supercooling of water that was forced up steep valley walls. The radar sounding data for Dome A (Figs. 2 and 3 in Bell et al., 2011) indicates that the production of subglacial water occurs at an $H$ of approximately 2900 m, which is slightly thicker than the case of the present study at DF (approximately 2800 m). Thus, for locations with $H >\sim 2900$ m, the bed is presumably temperate and very old ice strata at the bottom of the ice sheet are melted, causing refreezing in the surrounding area with thinner $H$. A contrasting aspect between Dome Fuji and Dome A is that, beneath Dome A, widespread Gamburtsev subglacial mountains have smaller $H$ ($>\sim 1500$ m) and thus any water produced has a limited number of paths within the subglacial mountain ranges through which to drain. Near DF, the area of the subglacial mountains is smaller and the elevation of the subglacial mountains is lower (with $H >\sim 2000$ m). Melted water refreezes beneath Dome A while melted water is drained at DF, considering the bed topography (Fig. 11). We examine the possibility of the existence/absence of refrozen ice near Dome Fuji. We argue that this dome-shaped deep ice is frozen to bed. However, it is not ice that once melted at the bottom of the ice sheet and refroze to lift up upper ice masses. It is because the deepest isochronous layer (yellow layer L4 near the bed in Fig. 13) has high integrity with respect to the upper isochronous layers. Layers L1 through L4





TCD
6, 1781–1837, 2012



have quite good integrity. In addition, refrozen ice is thin (<∼ 50 m) above subglacial mountains at Dome A (Figs. 2 and 3 in Bell et al., 2011). We find no such features in ice near DF. In the case of Dome C, based on Fig. 4 in Zirizzotti et al. (2012), the surface elevation is approximately 3230 m and the critical $H$ is approximately 2950 m. The boundary between the temperate bed and the frozen bed is deeper than that of both DF and Dome A. This may indicate that the geothermal heat flux near Dome C is smaller than that near DF, as suggested by the models of geothermal heat flux (Pollard et al., 2005; Shapiro and Ritzwoller, 2004).

## 5 Concluding remarks

Based on observations of the radar signal, we discussed the zones of water production at the ice/substrate interfaces in DML over distances of more than ∼ 3300 km. Both methods of diagnosis and data are useful for clarifying subglacial environments, in particular, as one of the boundary conditions in the ice sheet modelling to analyze temperature field and geothermal heat flux (e.g., Pattyn, 2010). Future efforts should include the compilation of a map for subglacial conditions, similar to the BEDMAP bed elevation map (Lythe et al., 2001).

The proposed method has an advantage compared to other methods for obtaining accurate reflectivity at the bottom of the ice sheet. Since the proposed method does not require accurate estimation of the temperature field within the ice or the impurity content within the ice, the diagnosis method is free from the errors related to these estimations. Although there are still unavoidable sources of error, such as the accumulation rate and geothermal flux anomalies (Matsuoka et al., 2011), the effect of birefringence, and interface roughness, these potential sources of errors are a more serious problem for the derivation of accurate reflectivity. The proposed method has fewer sources of errors, and is thus practical, with a small uncertainty estimated as several percent.

Based on the new data, we believe that the actual zones for melt water production are far wider than the known local areas of subglacial lakes. The empirical relations





TCD
6, 1781–1837, 2012



of surface elevation and ice thickness (Fig. 12) provide a hint for estimating the actual zones for melt water production. Ice sheet modelling using the results of the present study as the boundary conditions will be useful for improving our understanding of subglacial conditions. The existence of subglacial lakes indicates the existence of topographic troughs that are capable of preserving water within the vast zone of water production below the temperature of the pressure melting point. Bed topography map in DML (Fig. 11) indicates that vast areas have bed rock elevations lower than our routes. Therefore, except for coastal areas and high subglacial mountains, temperate subglacial conditions are dominant in DML.

We believe that the distribution of frozen bed near the coast has a strong impact on the ice discharge regime near the coast. Local basal melting above former rivers appears to be continuing because of water production from upstream inland. Except for such water discharge paths, the remaining areas near the coast are basically frozen to bedrock.

We found that two deep ice coring sites at Dome Fuji and EPICA-DML were within the zones of subglacial water production. Thicker ice inland of the ice sheet indicates that the base is at the pressure melting point, which means that, in order to access older ice, we should carefully avoid sites with thicker ice that may melt at the base. Near DF, Dome A, and Dome C, ice thickness $H$ of approximately 2800 m, 2900 m, and 2950 m is the critical thickness to reach the pressure melting point, respectively. Differences in the critical thickness may result from differences in geothermal heat flux. We proposed a candidate area for future ice coring on large subglacial mountains near DF. The ice in this area may contain very old ice strata in DML. Identifying the date of very deep ice is a challenge in paleoclimatic studies.

Temperate conditions at the bed are favourable for ice thickness detection by radar because the bed reflectivity increases by up to approximately 20 dB. Without basal melting, our ability to measure ice thickness is dramatically reduced.

The proposed diagnosis procedures should be useful for examining other areas of polar ice sheets. The possible errors by several percent are quite acceptable





TCD
6, 1781–1837, 2012



considering the scientific benefit of the diagnosis. In addition, we believe that the error rate cannot be reduced easily, even if the ice temperature field is modelled. The very long traceable 73.3 (±4) kyr BP isochrone, which is presumably associated with acidic layers due to the Toba supereruption, should also be useful for assessing ice flow conditions over the entire Antarctic continent. Using these layers, we will be able to better understand the subglacial conditions and identify more candidate locations for future ice coring.

*Acknowledgements.* The JASE traverse was organized by several organizations in Sweden and Japan. The National Institute of Polar Research (NIPR), Tokyo and the Swedish Polar Research Secretariat (SPRS) managed the logistics in Antarctica. Science management was a collaborative effort between NIPR, Stockholm University, the Royal Institute of Technology in Stockholm, and individuals from several universities and institutes in Japan. The JASE traverse is a research project of the Japanese Antarctic Research Expedition "Studies on systems for climate change and ice sheet change, by introducing new observational methods and technologies". The present study has been carried out under the umbrella of TASTE-IDEA within the framework of IPY project 152. The present study is also a contribution to IPICS and ITASE. The traverse was fully supported by the teams of the 48th and the 49th Japanese Antarctic Research Expeditions led by H. Miyaoka and S. Imura, respectively. Special thanks are to all the traverse members, for their very generous support during the traverse. The production of the present paper was supported by an NIPR publication subsidy. The present research was supported by a Grant-in-Aid for Scientific Research (A) 20241007 from the Japan Society for the Promotion of Science (JSPS).

## References

Bamber, J. L., Vaughan, D. G., and Joughin, I.: Widespread complex flow in the interior of the Antarctic ice sheet, Science, 287, 1248–1250, doi:10.1126/science.287.5456.1248, 2000. 1783, 1808

Bamber, J. L., Ferraccioli, F., Joughin, I., Shepherd, T., Rippin, D. M., Siegert, M. J., and Vaughan, D. G.: East Antarctic ice stream tributary underlain by major sedimentary basin, Geology, 34, 33–36, doi:10.1130/G22160.1, 2006. 1783, 1808





TCD
6, 1781–1837, 2012



Bamber, J. L., Gomez-Dans, J. L., and Griggs, J. A.: Antarctic 1 km Digital Elevation Model (DEM) from combined ERS-1 radar and ICESat Laser satellite altimetry, in: National Snow and Ice Data Center, Digital media, Boulder, Colorado, USA, 2009. 1786

Bell, R. E., Ferraccioli, F., Creyts, T. T., Braaten, D., Corr, H., Das, I., Damaske, D., Frearson, N., Jordan, T., Rose, K., Studinger, M., and Wolovick, M.: Widespread persistent thickening of the East Antarctic ice sheet by freezing from the base, Science, 331, 1592–1595, doi:10.1126/science.1200109, 2011. 1810, 1811

Bennett, M. R.: Ice streams as the arteries of an ice sheet: their mechanics, stability and significance, Earth-Sci. Rev., 61, 309–339, doi:10.1016/s0012-8252(02)00130-7, 2003. 1783, 1808

Bentley, C. R., Lord, N., and Liu, C.: Radar reflections reveal a wet bed beneath stagnant ice stream C and a frozen bed beneath ridge BC, West Antarctica, J. Glaciol., 44, 149–156, 1998. 1784

Carter, S. P.: Radar-based subglacial lake classification in Antarctica, Geochem. Geophys. Geosyst., 8, Q03016, doi:10.1029/2006GC001408, 2007. 1784

Carter, S. P., Blankenship, D. D., Young, D. A., and Holt, J. W.: Using radar-sounding data to identify the distribution and sources of subglacial water: application to Dome C, East Antarctica, J. Glaciol., 55, 1025–1040, doi:10.3189/002214309790794931, 2009. 1784

Chesner, C. A., Rose, W. I., Deino, A., Drake, R., and Westgate, J. A.: Eruptive history of Earth's largest Quaternary caldera (Toba, Indonesia) clarified, Geology, 19, 200–203, doi:10.1130/0091-7613(1991)019<0200:EHOESL>2.3.CO;2, 1991. 1792

Cuffey, K. M. and Paterson, W. S. B.: The Physics of Glaciers, 4 Edn., Academic Press, 704 pp., ISBN-10:0123694612, ISBN-13:978-0123694614, 2010. 1804

Fujita, S., Maeno, H., Uratsuka, S., Furukawa, T., Mae, S., Fujii, Y., and Watanabe, O.: Nature of radio-echo layering in the Antarctic ice sheet detected by a two-frequency experiment, J. Geophys. Res., 104, 13013–13024, doi:10.1029/1999JB900034, 1999. 1785, 1786, 1790, 1810, 1826

Fujita, S., Matsuoka, T., Ishida, T., Matsuoka, K., and Mae, S.: A summary of the complex dielectric permittivity of ice in the megahertz range and its applications for radar sounding, in: Physics of Ice Core Records, edited by: Hondoh, T., Hokkaido University Press, Sapporo, 185–212, 2000. 1788

Fujita, S., Maeno, H., Furukawa, T., and Matsuoka, K.: Scattering of VHF radio waves from within the top 700 m of the Antarctic ice sheet and its relation to the depositional environ-





TCD
6, 1781–1837, 2012



ment: a case study along the Syowa-Mizuho-Dome F traverse, Ann. Glaciol., 34, 157–164, doi:10.3189/172756402781817888, 2002. 1785, 1790, 1806
Fujita, S., Maeno, H., and Matsuoka, K.: Radio-wave depolarization and scattering within ice sheets: a matrix-based model to link radar and ice-core measurements and its application, J. Glaciol., 52, 407–424, doi:10.3189/172756506781828548, 2006. 1788
Fujita, S., Holmlund, P., Andersson, I., Brown, I., Enomoto, H., Fujii, Y., Fujita, K., Fukui, K., Furukawa, T., Hansson, M., Hara, K., Hoshina, Y., Igarashi, M., Iizuka, Y., Imura, S., Ingvander, S., Karlin, T., Motoyama, H., Nakazawa, F., Oerter, H., Sjöberg, L. E., Sugiyama, S., Surdyk, S., Ström, J., Uemura, R., and Wilhelms, F.: Spatial and temporal variability of snow accumulation rate on the East Antarctic ice divide between Dome Fuji and EPICA DML, The Cryosphere, 5, 1057–1081, doi:10.5194/tc-5-1057-2011, 2011. 1785, 1786, 1825, 1826
Haran, T., Bohlander, J., Scambos, T., Painter, T., and Fahnestock, M.: MODIS mosaic of Antarctica (MOA) image map, in: National Snow and Ice Data Center, Digital media, Boulder, Colorado, USA, 2005, updated 2006. 1825
Holmlund, P. and Fujita, S.: Japanese-Swedish Antarctic Expedition JASE, in: Swedish Polar Secretariat Year Book 2008, edited by: Thorén A., Swedish Polar Research Secretariat, Stockholm, 18, 2009. 1785, 1825
Huybrechts, P., Rybak, O., Pattyn, F., and Steinhage, D.: Past and present accumulation rate reconstruction along the Dome Fuji-Kohnen radio echo sounding profile, Dronning Maud Land, East Antarctica, Ann. Glaciol., 50, 112–120, doi:10.3189/172756409789097513, 2009. 1791, 1792, 1826, 1836
Hvidberg, C. S.: Steady-state thermomechanical modelling of ice flow near the centre of large ice sheets with the finite element technique, Ann. Glaciol., 23, 116–123, 1996. 1791, 1802
Jacobel, R., Welch, B. C., Osterhouse, D., Pettersson, R., and MacGregor, J. A.: Spatial variation of radar-derived basal conditions on Kamb Ice Stream, West Antarctica, Ann. Glaciol., 50, 10–16, doi:10.3189/172756409789097504, 2009. 1784
Jouzel, J. and Masson-Delmotte, V.: Deep ice cores: the need for going back in time, Quaternary Sci. Rev., 29, 3683–3689, doi:10.1016/j.quascirev.2010.10.002, 2010. 1783, 1808
Langley, K., Kohler, J., Matsuoka, K., Sinisalo, A., Scambos, T., Neumann, T., Muto, A., Winther, J. G., and Albert, M.: Recovery lakes, East Antarctica: radar assessment of subglacial water extent, Geophys. Res. Lett., 38, L05501, doi:10.1029/2010GL046094, 2010. 1784





TCD
6, 1781–1837, 2012



Lythe, M. B., Vaughan, D. G., and the BEDMAP consortium: BEDMAP: a new ice thickness and subglacial topographic model of Antarctica, J. Geophys. Res., 106, 11335–11351, doi:10.1029/2000JB900449, 2001. 1811, 1835

MacGregor, J. A., Winebrenner, D. P., Conway, H., Matsuoka, K., Mayewski, P. A., and Clow, G. D.: Modeling englacial radar attenuation at Siple Dome, West Antarctica, using ice chemistry and temperature data, J. Geophys. Res.-Earth, 112, F03008, doi:10.1029/2006JF000717, 2007. 1784

Mae, S. and Naruse, R.: Possible causes of ice sheet thinning in the Mizuho Plateau, Nature, 273, 291–292, doi:10.1038/273291a0, 1978. 1804

Matsuoka, K.: Pitfalls in radar diagnosis of ice-sheet bed conditions: Lessons from englacial attenuation models, Geophys. Res. Lett., 38, L05505, doi:10.1029/2010GL046205, 2011. 1784, 1788, 1789, 1800, 1805, 1811

Matsuoka, K., Maeno, H., Uratsuka, S., Fujita, S., Furukawa, T., and Watanabe, O.: A ground-based, multi-frequency ice-penetrating radar system, Ann. Glaciol., 34, 171–176, doi:10.3189/172756402781817400, 2002. 1786

Matsuoka, K., Wilen, L., Hurley, S. P., and Raymond, C. F.: Effects of birefringence within ice sheets on obliquely propagating radio waves, IEEE T. Geosci. Remote, 47, 1429–1443, doi:10.1109/TGRS.2008.2005201, 2009. 1788

Motoyama, H.: The second deep ice coring Project at Dome Fuji, Antarctica, Scientific Drilling, 5, 41–43, doi:10.2204/iodp.sd.5.05.2007, 2007. 1785, 1808, 1809

Motoyama, H., Enomoto, H., Furukawa, T., Kamiyama, K., Shoji, H., Shiraiwa, T., Watanabe, K., Namasu, K., and Ikeda, H.: Preliminary study of ice flow observations along traverse routes from coast to Dome Fuji, East Antarctica by differential GPS method, Nankyoku Shiryo (Antarctic Record), 39, 94–98, 1995. 1792, 1804, 1806, 1830

Motoyama, H. and Dome Fuji ice core project members: a new 3035.22 m deep ice core at Dome Fuji, Antarctica and reconstruction of global climate and environmental change over past 720 kyr, Eos Trans. AGU, 88, Fall Meet. Suppl., Abstract C51A-0076, 2007. 1785, 1809

Motoyama, H., Furukawa, T., and Nishio, F.: Study of ice flow observations in Shirase drainage basin and around Dome Fuji area, East Antarctica by differential GPS method, Nankyoku Shiryo (Antarctic Record), 52, 216–231, 2008 (in Japanese). 1791

Murshed, M. M., Faria, S. H., Kuhs, W. F., Kipfstuhl, S., and Wilhelms, F.: The role of hydrochlorofluorocarbon densifiers in the formation of clathrate hydrates in deep boreholes and sub-





TCD
6, 1781–1837, 2012



glacial environments, Ann. Glaciol., 47, 109–114, doi:10.3189/172756407786857659, 2007. 1785, 1803, 1808

Näslund, J. O., Fastook, J. L., and Holmlund, P.: Numerical modelling of the ice sheet in Western Dronning Maud Land, East Antarctica: impacts of present, past and future climates, J. Glaciol., 46, 54–66, doi:10.3189/172756500781833331, 2000. 1792, 1796

Ninkovich, D., Shackleton, N. J., Abdelmonem, A. A., Obradovich, J. D., and Izett, G.: K-Ar age of late Pleistocene eruption of Toba, North Sumatra, Nature, 276, 574–577, doi:10.1038/276574a0, 1978. 1792

Nishio, F. and Mae, S.: Temperature profile in the bare ice area near the Yamato Mountains, Antarctica, Mem. Natl Inst. Polar Res. Spec. Issue, 12, 25–37, 1979. 1804

Oerter, H., Graf, W., Meyer, H., and Wilhelms, F.: The EPICA ice core from Dronning Maud Land: first results from stable-isotope measurements, Ann. Glaciol., 39, 307–312, doi:10.3189/172756404781814032, 2004. 1785

Parrenin, F., Dreyfus, G., Durand, G., Fujita, S., Gagliardini, O., Gillet, F., Jouzel, J., Kawamura, K., Lhomme, N., Masson-Delmotte, V., Ritz, C., Schwander, J., Shoji, H., Uemura, R., Watanabe, O., and Yoshida, N.: 1-D-ice flow modelling at EPICA Dome C and Dome Fuji, East Antarctica, Clim. Past, 3, 243–259, doi:10.5194/cp-3-243-2007, 2007. 1792

Pattyn, F.: Antarctic subglacial conditions inferred from a hybrid ice sheet/ice stream model, Earth Planet. Sc. Lett., 295, 451–461, doi:10.1016/j.epsl.2010.04.025, 2010. 1783, 1784, 1799, 1807, 1809, 1811

Pattyn, F. and Decleir, H.: Numerical sumulation of Shirase Glacier, East Queen Maud Land, Antarctica Proc. NIPR Symp. Polar Meteor. Glaciol., 9, 87–109, 1995. 1805

Pattyn, F., De Brabander, S., and Huyghe, A.: Basal and thermal control mechanisms of the Ragnhild glaciers, East Antarctica, in: Annals of Glaciology, vol. 40, edited by: MacAyeal, D. R., Int. Glaciological Soc., Cambridge, 225–231, doi:10.3189/172756405781813672, 2005. 1783, 1808

Peters, M. E., Blankenship, D. D., and Morse, D. L.: Analysis techniques for coherent airborne radar sounding: application to West Antarctic ice streams, J. Geophys. Res., 110, B06303, doi:10.1029/2004JB003222, 2005. 1784, 1787

Pollard, D., DeConto, R. M., and Nyblade, A. A.: Sensitivity of Cenozoic Antarctic ice sheet variations to geothermal heat flux, Global Planet. Change, 49, 63–74, doi:10.1016/j.gloplacha.2005.05.003, 2005. 1811





TCD
6, 1781–1837, 2012



Popov, S. V. and Masolov, V. N.: Forty-seven new subglacial lakes in the 0–110° E sector of East Antarctica, J. Glaciol., 53, 289–297, doi:10.3189/172756507782202856, 2007. 1784, 1785, 1794, 1795, 1803

Priscu, J. C., Tulaczyk, S., Studinger, M., II, M. C. K., Christner, B. C., and Foreman, C. M.: Antarctic subglacial water: origin, evolution, and ecology, in: Polar Lakes and Rivers: Limnology of Arctic and Antarctic Aquatic Ecosystems, edited by: Vincent, W. F. and Laybourn-Parry, J., Oxford University Press, USA, 320, doi:10.1093/acprof:oso/9780199213887.003.0007, 2008. 1782

Rémy, F., Testut, L., Legrésy, B., Forieri, A., Bianchi, C., and Tabacco, I. E.: Lakes and subglacial hydrological networks around Dome C, East Antarctica, Ann. Glaciol., 37, 252–256, doi:10.3189/172756403781815799, 2003. 1782

Ray, P. S.: Broadband complex refractive indices of ice and water, Appl. Opt., 11, 1836–1844, doi:10.1364/A O.11.001836, 1972. 1787

Raymond, C. F.: Deformation in the vicinity of ice devide, J. Glaciol., 29, 357–373, 1983. 1791, 1802

Rignot, E., Mouginot, J., and Scheuchl, B.: Ice flow of the Antarctic ice sheet, Science, 333, 1427–1430, doi:10.1126/science.1208336, 2011. 1783, 1808

Ruth, U., Barnola, J.-M., Beer, J., Bigler, M., Blunier, T., Castellano, E., Fischer, H., Fundel, F., Huybrechts, P., Kaufmann, P., Kipfstuhl, S., Lambrecht, A., Morganti, A., Oerter, H., Parrenin, F., Rybak, O., Severi, M., Udisti, R., Wilhelms, F., and Wolff, E.: "EDML1": a chronology for the EPICA deep ice core from Dronning Maud Land, Antarctica, over the last 150 000 years, Clim. Past, 3, 475–484, doi:10.5194/cp-3-475-2007, 2007. 1792

Rybak, O., Huybrechts, P., Pattyn, F., and Steinhage, D.: Regional ice-dynamic model, Part 1. model description, performance of numerical experiments, and present-day ice-flow dynamics around Kohnen station, Materialy Gliatsiologitcheskikh Issledovanij, 102, 3–11, 2007 (in Russian). 1791

Saito, F. and Abe-Ouchi, A.: Thermal structure of Dome Fuji and East Dronning Maud Land, Antarctica, simulated by a three-dimensional ice-sheet model, Ann. Glaciol., 39, 433–438, doi:10.3189/172756404781814258, 2004. 1805

Sawagaki, T. and Hirakawa, K.: Erosion of bedrock by subglacial meltwater, Soya Coast, East Antarctica, Geogr. Ann. A, 79, 223–238, doi:10.1111/j.0435-3676.1997.00019.x, 1997. 1797





TCD
6, 1781–1837, 2012



Sawagaki, T. and Hirakawa, K.: Hydrostatic investigations on subglacial meltwater: implications for the formation of streamlined bedforms and subglacial lakes, East Antarctica, Polar Geosci., 15, 123–147, 2002. 1797

Seddik, H., Greve, R., Zwinger, T., and Placidi, L.: A full Stokes ice flow model for the vicinity of Dome Fuji, Antarctica, with induced anisotropy and fabric evolution, The Cryosphere, 5, 495–508, doi:10.5194/tc-5-495-2011, 2011. 1791, 1809

Shapiro, N. M. and Ritzwoller, M. H.: Inferring surface heat flux distributions guided by a global seismic model: particular application to Antarctica, Earth Planet. Sc. Lett., 223, 213–224, doi:10.1016/j.epsl.2004.04.011, 2004. 1811

Siegert, M. J., Carter, S., Tabacco, I., Popov, S., and Blankenship, D.: A revised inventory of Antarctic subglacial lakes, Antarct. Sci., 17, 453–460, doi:10.1017/S0954102005002889, 2005. 1784

Siegert, M. J., II, M. C. K., and Bindschadler, R. A.: Antarctic Subglacial Aquatic Environments, Geophysical Monograph Series AGU, 246 pp., ISBN: 978-0-87590-482-5, 2011. 1782

Smith, B. E., Fricker, H. A., Joughin, I. R., and Tulaczyk, S.: An inventory of active subglacial lakes in Antarctica detected by ICESat (2003–2008), J. Glaciol., 55, 573–595, doi:10.3189/002214309789470879, 2009. 1784

Watanabe, O., Kamiyama, K., Motoyama, H., Fujii, Y., Shoji, H., and Satow, K.: The paleoclimate record in the ice core at Dome Fuji Station, East Antarctica, Ann. Glaciol., 29, 176–178, doi:10.3189/172756499781821553, 1999. 1785

Wesche, C., Eisen, O., Oerter, H., Schulte, D., and Steinhage, D.: Surface topography and ice flow in the vicinity of the EDML deep-drilling site, Antarctica, J. Glaciol., 53, 442–448, doi:10.3189/002214307783258512, 2007. 1791

Wolff, E., Brook, E., Dahl-Jensen, D., Fujii, Y., Jouzel, J., Lipenkov, V., and Severinghaus, J.: The oldest ice core: a 1.5 million year record of climate and greenhouse gases from Antarctica, International Partnerships in Ice Core Sciences, available online: http://www.pages-igbp.org/ipics/data/ipics_oldaa.pdf, 2006. 1783, 1808

Zirizzotti, A., Cafarella, L., Baskaradas, J. A., Tabacco, I. E., Urbini, S., Mangialetti, M., and Bianchi, C.: Dry-wet bedrock interface detection by radio echo sounding measurements, IEEE T. Geosci. Remote, 48, 2343–2348, doi:10.1109/TGRS.2009.2038900, 2010. 1784

Zirizzotti, A., Cafarella, L., and Urbini, S.: Ice and bedrock characteristics underneath Dome C (Antarctica) from radio echo sounding data analysis, IEEE T. Geosci. Remote, 50, 37–43, doi:10.1109/TGRS.2011.2160551, 2012. 1784, 1811





TCD
6, 1781–1837, 2012



**Table 1.** Settings of VHF radar systems used to detect bed returned power signals.

| Name of radar | 179-1 | 179-2 | 60 |
|---|---|---|---|
| Carrier frequency | 179 MHz | 179 MHz | 60 MHz |
| Transmitter pulse width | 500 ns | 350 ns/1000 ns | 250 ns/1000 ns |
| Noise floor | −115 dBm[a] | −115 dBm | −115 dBm |
| Antenna type | 3-element Yagi | 3 element Yagi | 3-element Yagi |
| Antenna gain | 8.2 dBi[b] | 8.15 dBi | 7.2 dBi |
| Vertical resolution in ice[c] | 42 m | 30 m/89 m | 21 m/85 m |
| Wavelength in ice | 0.94 m | 0.94 m | 2.8 m |
| Observed legs and used pulse width[d] | A1 (500 ns) | A1, A2, A3 (350 ns) | A1, A2 (250 ns), A3 (250 and 1000 ns) |
| | B1, B2 (500 ns) | – | B1, B2 (1000 ns) |
| | C1 (500 ns) | C2 (1000 ns), C3 (500 ns) | C2 (1000 ns) |
| | – | D (1000 ns) | – |
| | – | E1 (1000 ns) | E2 (250 ns) |
| | – | – | F1, F2 (250 ns) |

[a] dBm is a unit of power level in decibels with reference to a power of 1 mW. Receiver sensitivity assumes averaging to reduce the noise level.
[b] dBi is a unit of antenna gain in decibels with reference to the power of an ideal isotropic antenna.
[c] Vertical resolutions are the wave travel distances for half of the pulse width.
[d] Numbers in brackets show pulse width used in each leg. See text.





TCD
6, 1781–1837, 2012



**Table 2.** Major sites along the inland traverse.

| Site Name | Lat. ° S | Long. °[a] | Elevation (m) | $H$ (m)[b] | Legs[c] | Note |
|---|---|---|---|---|---|---|
| S16 | 69.030 | 40.052 | 589 | 350 | E2 | Base of the Japanese team near the coast |
| H176 | 69.575 | 41.961 | 1543 | 1510 | E2 | Northern side of the temperate bed upstream of the Soya Coast |
| H270 | 69.909 | 42.781 | 1794 | 1450 | E2 | Southern side of the temperate bed upstream of the Soya Coast |
| Mizuho | 70.697 | 44.274 | 2250 | 2060 | E2 | |
| MD170 | 72.273 | 43.728 | 2749 | 2335 | E2, F2 | |
| MD384 | 74.185 | 42.886 | 3381 | 2381 | F1, F2 | |
| MD585 | 75.983 | 41.194 | 3679 | 2078 | A1, F1 | |
| DF | 77.317 | 39.703 | 3800 | 3028 | A1, A2, B1, C1 | Dome Fuji Station. 3035-m long ice coring site |
| SSW47 | 77.801 | 39.04 | 3761 | 2157 | A2 | Site above subglacial mountains |
| SSW90 | 78.164 | 38.538 | 3709 | 2661 | A2 | Site above high-shearing above subglacial mountains |
| SSW150 | 78.683 | 37.795 | 3656 | 3124 | A2 | Southernmost point of the survey in 1996/1997 season |
| DF80 | 77.373 | 39.617 | 3798 | 2790 | A2, A3 | End point of the leg A3 |
| East95 | 77.363 | 43.568 | 3714 | 3027 | A3 | Subglacial Lake Point |
| East130 | 77.361 | 45.01 | 3669 | 2274 | A3 | Easternmost point of the survey in 1996/1997 season |
| RT441 | 77.498 | 37.428 | 3770 | 3154 | B1 | Subglacial Lake Point |
| RT313 | 77.961 | 32.624 | 3620 | 3249 | B1, B2 | Subglacial Lake Point |
| RT188 | 77.161 | 29.426 | 3678 | 2473 | B2 | One of the corners of the leg |
| RT155 | 76.869 | 29.270 | 3701 | 2601 | B2 | One of the corners of the leg |
| MP: meeting point | 75.888 | 25.834 | 3661 | 2792 | B2, B3, C1, C2 | Meeting point of the two national teams |
| NCR62 | 75.428 | 27.153 | 3589 | 2772 | B3 | Northernmost point of the cross-ridge traverse at the meeting point |
| A38 | 75.287 | 18.421 | 3543 | 2706 | C2 | |
| A28 | 74.862 | 14.742 | 3466 | – | C2, C3 | End point of the leg C2 |
| EPICA DML (Kohnen) | 75.004 | −0.006 | 2890 | 2774 | C3, D | 2774-m deep ice coring site |
| IPY Site1 | 75.001 | −10.121 | 2528 | 1603 | D, E1 | Science stopping point |
| – | 74.454 | −11.572 | 1078 | 1689 | E1 | Southern side of the Veststraumen Ice Stream |
| – | 74.046 | −12.006 | 998 | 1591 | E1 | Northern side of the Veststraumen Ice Stream |
| Wasa Station | 73.053 | −13.374 | 292 | 383 | E1 | Base of the Swedish Team |

[a] Positive and negative longitudes indicate east and west, respectively.
[b] $H$: ice thickness (m).
[c] Legs including the site.





TCD
6, 1781–1837, 2012



**Table 3.** Segments analyzed in this study.

| ID | Sites at both both ends of segments | Distance (km) | Range of $H$ (m) | Range of surface elevation (m) | Range of annual accumulation rate ($kg\,m^{-2}\,yr^{-1}$) |
|---|---|---|---|---|---|
| A1 | MD585–DF | 151 | 2040–3450 | 3680–3800 | 20–40 |
| A2 | DF–SSW150 | 156 | 2050–3430 | 3800–3650 | 20–30 |
| A3 | DF80–East135 | 130 | 2200–3220 | 3800–3670 | 20–30 |
| B1 | DF–RT313 | 205 | 2270–3400 | 3800–3620 | 20–30 |
| B2 | RT313–MP | 312 | 1780–3450 | 3620–3660 | 20–40 |
| B3 | MP–NCR62 | 62 | 2250–3020 | 3660–3590 | 30–40 |
| C1 | DF–DK261 | 403 | 2200–3300 | 3800–3710 | 20–40 |
| C2 | MP–A38 | 333 | 2220–2970 | 3660–3540 | 30–40 |
| D | EPICA DML–Site 1 | 310 | 800–2900 | 2890–2530 | 40–100 |
| E1 | Site 1–Wasa | 353 | < 100–1900 | 2100–290 | 100–370 |
| E2 | S16–MD170 | 437 | 300–2650 | 590–2750 | 80–140 |
| F1 | MD585–MD384 | 205 | 2040–3350 | 3680–3390 | 40–60 |
| F2 | MD384–MD170 | 214 | 1780–2860 | 3390–2750 | 0–80 |





TCD
6, 1781–1837, 2012



**Table 4.** Gradients obtained from linear regression analyses.

| Leg ID | Range and span of $H$ (m) | $< N >$: Half of gradient of regression line (dB km$^{-1}$)[a] | Corresponding ice temperature (°C)[b] |
|---|---|---|---|
| A | 2050–2600 (550) | −12 (±1) | −20 |
| B | 1900–2600 (700) | −15 (±1) | −18 |
| D | 1500–2500 (900) | −19 (±1) | −15 |
| E1 | 700–1150 (550) | −22 (±1) | −12 |
| E2 | 750–1250 (500) | −21 (±1) | −13 |
| F1 | 2050–2370 (320) | −12 (±3) | −20 |

[a] These values are for one-way wave propagation, assuming they are approximate values of the attenuation coefficient (dB km$^{-1}$). These values cannot be accurate values of the attenuation coefficient if spatial variations of the bed reflectivity exist.

[b] The estimated attenuation coefficients were converted to corresponding ice temperature assuming that the ice contain a small amount (~ 2 μM) of acidity. See Fig. 9c in Fujita et al. (2000).





TCD
6, 1781–1837, 2012



**Table 5.** Methods of diagnosis and results for each leg.

| ID | Methods[a] | Distance (km) diagnozed as temperate bed | Distance (km) diagnozed as frozen bed | Estimated maximum distance (km) of possible misjudgment | Distance (km) for undetected ice thickness |
|---|---|---|---|---|---|
| A1 | 1–3 | 133.3 | 17.3 | 3.8 | 0.0 |
| A2 | 1–3 | 67.7 | 88.3 | 3.9 | 0.0 |
| A3 | 1–3 | 98.7 | 31.3 | 3.3 | 0.0 |
| B1 | 1–3 | 168.5 | 19.8 | 4.7 | 16.7 |
| B2 | 1–3 | 164.6 | 53.3 | 5.4 | 94.1 |
| B3 | 1–3 | 34.0 | 10.7 | 1.1 | 17.4 |
| C1 | 1–4 | 208.3 | 27.9 | 5.9 | 172.5 |
| C2 | 1–4 | 190 | 0.0 | 4.7 | 144 |
| D | 1–3 | 138.8 | 154.1 | 7.3 | 17.4 |
| E1 | 1–3 | 109.7 | 232.1 | 10.7 | 11.1 |
| E2 | 1–3 | 321.9 | 91.9 | 10.2 | 22.7 |
| F1 | 1–4 | 186.3 | 18.3 | 8.2 | 0.0 |
| F2 | only 4 | 214.1 | 0.0 | 13.3[b] | 0.0 |
| | Total (km) | 2035.6 | 745.0 | 82.6 | 495.6 |
| | Total (%) | 62 | 23 | 3 | 15 |

[a] Major steps used for the diagnosis. For legs C1, C2 and F1, step 4 was necessary, in addition to the steps 1–3. For leg F2, steps 1–3 were unavailable.
[b] This number reflects estimated ambiguity of the diagnosis in this leg.





TCD
6, 1781–1837, 2012



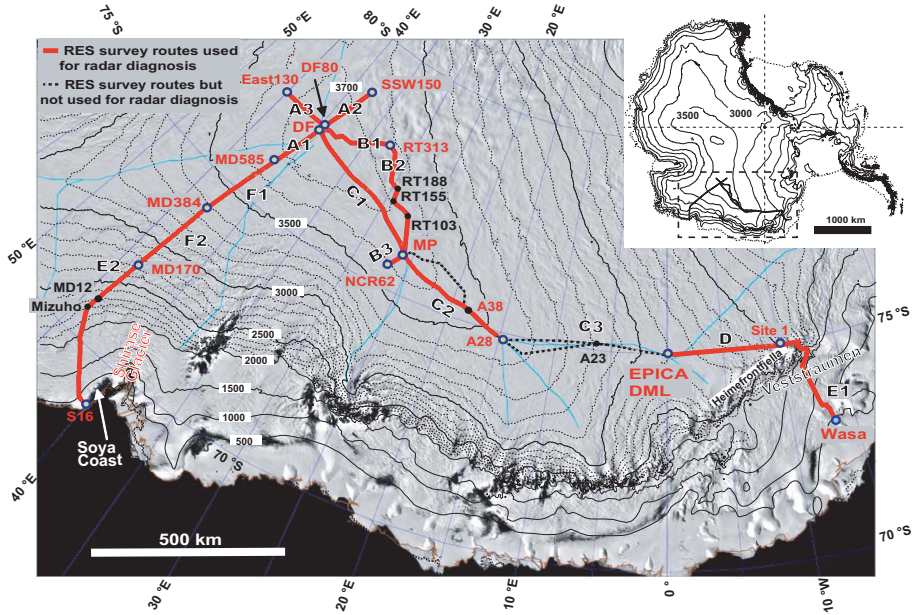


**Fig. 1.** Dronning Maud Land, East Antarctica. Contours show the surface elevation in meters relative to the WGS84 ellipsoid. The background satellite image is a MODIS mosaic of Antarctica (Haran et al., 2005). The red lines show the survey routes for the ground-based radar sounding discussed herein. The traces include a route of the JASE traverse (Holmlund and Fujita, 2009; Fujita et al., 2011) connecting two deep ice coring sites, namely, Dome Fuji and EPICA DML. The locations of major sites along the routes are listed in Table 2. Fourteen legs, labelled from A1 to F2, are listed in Table 3. The thin blue traces represent ice divides that separate drainage basins.





TCD
6, 1781–1837, 2012

Subglacial conditions in Dronning Maud Land, East Antarctica

S. Fujita et al.



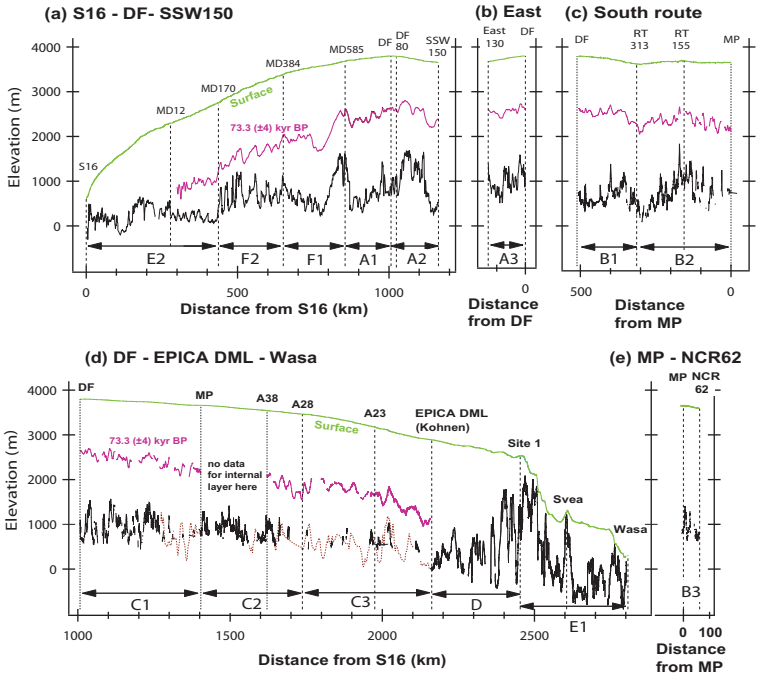


**Fig. 2.** Cross-sectional plot of the ice sheet. Fourteen legs, labelled, e.g., A1, are discussed herein. The abscissa indicates the horizontal distance along the profiles, and the ordinate indicates the elevation above the WGS84 ellipsoid. The vertical exaggeration is approximately 500 times. The locations of major sites reported in Table 2 are shown as vertical dashed lines. The bed elevation (black) was calculated from the surface elevation data and ice thickness data extracted from the radar sounding data (Fujita et al., 1999, 2011), and when this dataset does not show the bed reflection, the data are from Huybrechts et al. (2009) (brown). One of many traceable isochrones (englacial radar reflectors) in the radar sounding data is shown. The details of this isochrone are discussed in the text.





TCD
6, 1781–1837, 2012



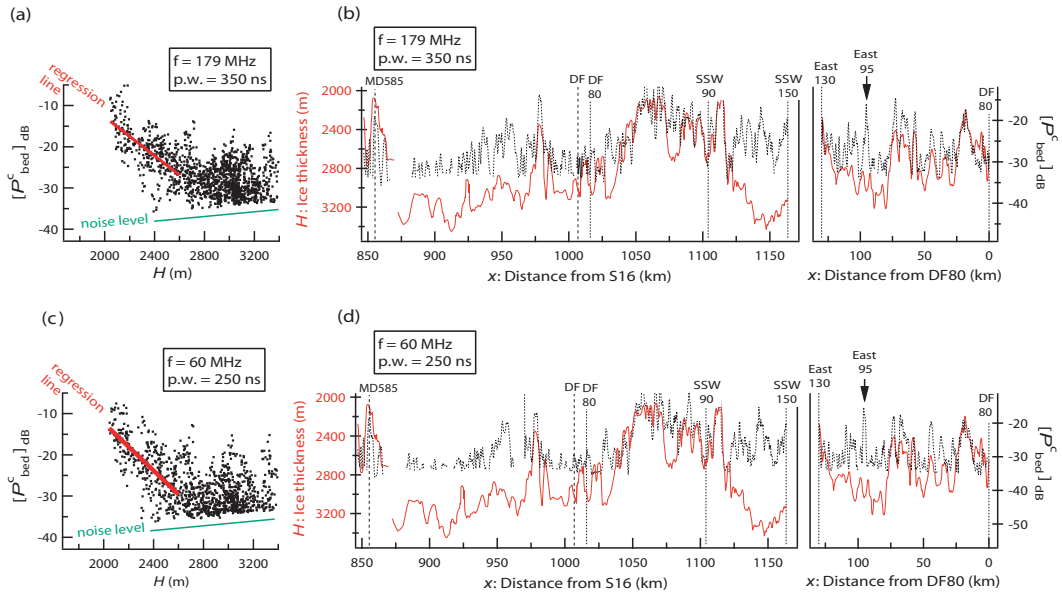


**Fig. 3.** Variation of the geometrically corrected return power from the bed $[P^c_{bed}]_{dB}$ (dB) in terms of ice thickness (**a**, **c**) and location (**b**, **d**), along the series A legs in the vicinity of Dome Fuji. The upper and lower rows show the data collected at radar frequencies of 60 MHz and 179 MHz, respectively. See the text for details.





TCD
6, 1781–1837, 2012



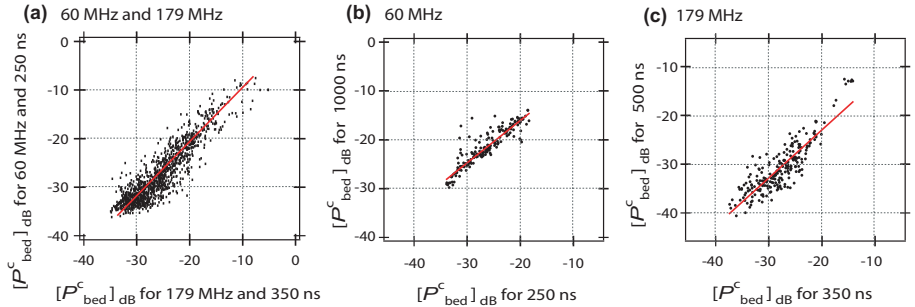


**Fig. 4.** Variations of $[P^c_{bed}]_{dB}$ versus ice thickness $H$ and location $x$ are virtually independent of the radar frequencies and radar pulse widths used in the present study. Three examples are shown. **(a)** For all of the data in Fig. 3 (legs A1 through A3), a scatter plot of the results for two different frequencies was produced. **(b)** Scatter plot of the results for two different radar pulse widths (1000 ns and 250 ns) for a radar frequency of 60 MHz for leg A3. **(c)** Scatter plot of the results for two different radar pulse widths (500 ns and 350 ns) for a radar frequency of 179 MHz for leg A1. A linear distribution was found for each of these scatter plots.





TCD
6, 1781–1837, 2012



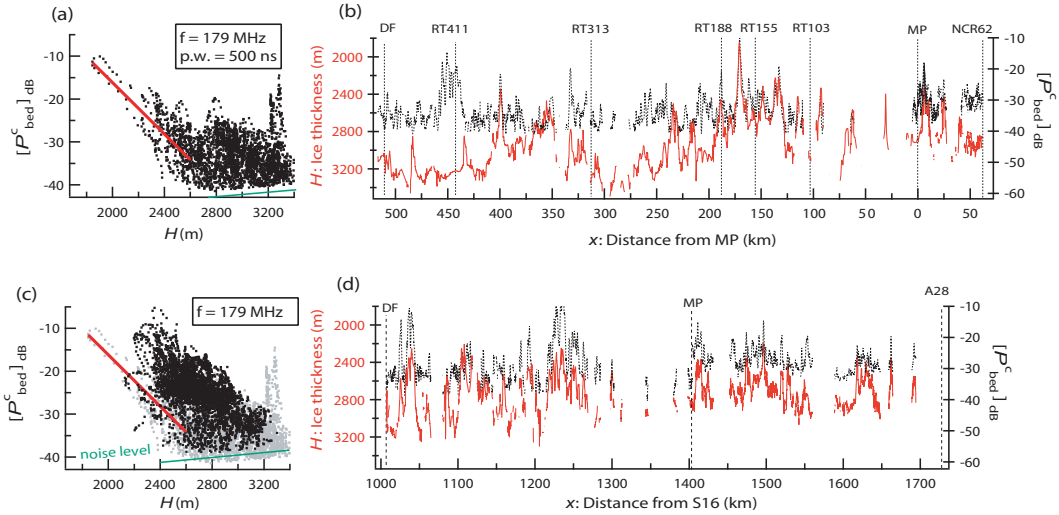


**Fig. 5.** Results for series B and C legs. **(a)** H-P plot along the series B legs for data using the 179-MHz radar. The red line is the regression line for $H$ of less than 2600 m. **(b)** X-PH plot for the same data. The regression line in **(a)** was used to obtain the scales of the left- and right-hand axes. **(c)** H-P plot along the series C legs for data using the 179-MHz radar. The black dots indicate the results along the series C legs. The grey dots in the background indicate the results for the series B neighbouring legs for comparison. The regression analysis is not appropriate for the series C legs because the legs are subject to a special ice flow condition along the exact ice divide known as the Raymond effect (see text). Smaller vertical advection makes the ice warmer locally. The regression line of **(a)** is shown as a reference. Based on a comparison of the series C and B legs, the temperature conditions in the series C legs are warmer than the temperature conditions in the series B legs. **(d)** X-PH plot along the series C legs.





TCD
6, 1781–1837, 2012



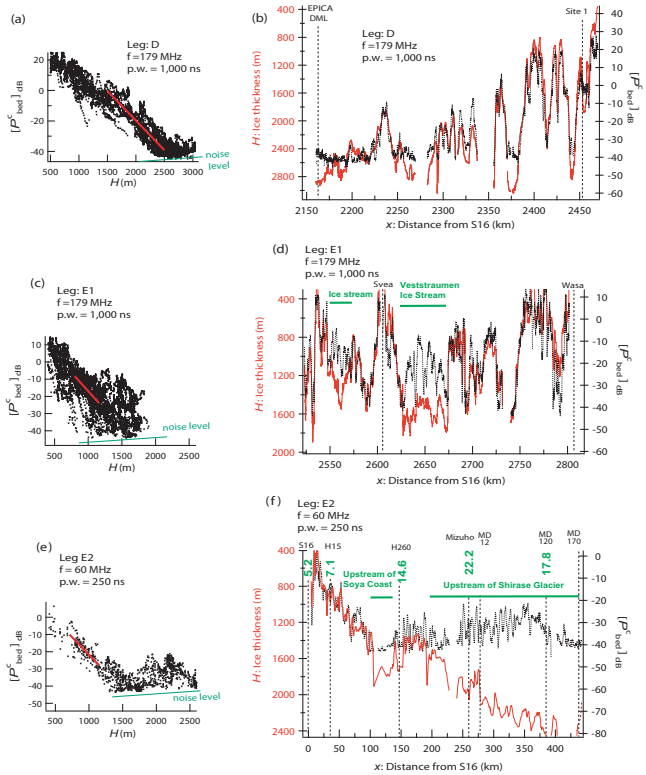


**Fig. 6.** Results along the series D and E legs. **(a)** H-P plot for leg D. The red line is the regression line to a depth of 2500 m. **(b)** X-PH plot for leg D, with scaling using the regression line in **(a)**. **(c)** H-P plot along leg E1. **(d)** X-PH plot along leg E1, with scaling using the regression line in **(c)**. The locations of the major ice streams are indicated. **(e)** H-P plot along leg E2. **(f)** X-PH plot along leg E2, with scaling using the regression line in **(e)**. The upstream area of the Soya Coast and the upstream area of the Shirase Glacier are indicated. Numbers with green letters indicates ice flow speeds ($m\,yr^{-1}$) (Motoyama et al., 1995).





TCD
6, 1781–1837, 2012



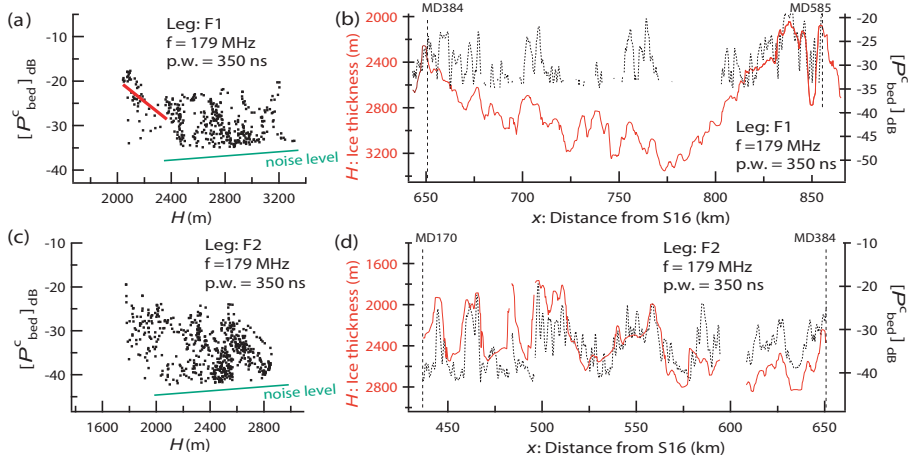


**Fig. 7.** Results along the series F legs. **(a)** H-P plot for leg F1. The red line is the regression line to a depth of 2360 m. **(b)** X-PH plot for leg F1, with scaling using the regression line in **(a)**. **(c)** H-P plot for leg F2. The regression line was not derived because it was not possible to define an appropriate range for this line. **(d)** X-PH plot for leg F1. The left- and right-hand axes were scaled and adjusted using the gradient of the regression line of F1.





TCD
6, 1781–1837, 2012



**STEP 1: *H-P* Plot diagnosis**

Possible conditions and expected features of data are as follows.

| | | |
|---|---|---|
| Only frozen conditions exist within a data set covering an area. | Frozen and temperate conditions co-exist within a data set covering an area. | Only temperate conditions exist within a data set covering an area. |
| $[P^{c}_{bed}]_{dB}$ decreases with increasing $H$. | $[P^{c}_{bed}]_{dB}$ decreases with increasing $H$. However, systematic increases of $[P^{c}_{bed}]_{dB}$ appear at $H$ larger than the critical value. | $[P^{c}_{bed}]_{dB}$ decreases with increasing $H$. However, this correlation can be highly obscured or erased by heterongeneously distributed water at the bed. |

**STEP 2: Radiowave attenuation range diagnosis**

We detemine the $[P^{c}_{bed}]_{dB}/H$ gradient at $H$ ranges smaller than the critical $H$ values. We must determine whether the $[P^{c}_{bed}]_{dB}/H$ gradient is within a range that is explicable by the attenuation coefficient of radiowaves within ice in an expected temperature range.

**STEP 3: *X-HP* Plot diagnosis**

Possible conditions and expected features of data are as follows.

| | | |
|---|---|---|
| Only frozen conditions exists within a data set covering an area. | Frozon and temperate conditions co-exist within a data set covering an area. | Only temperate conditions exist within a data set covering an area. |
| $[P^{c}_{bed}]_{dB}$ and $H$ are inversely correlated. | Breaks of the inverse correlation between $[P^{c}_{bed}]_{dB}$ and $H$ are found at $H$ larger than the critical $H$. | $[P^{c}_{bed}]_{dB}$ and $H$ have a weak inverse correlation. However, this correlation can be highly obscured or eliminated by heterongeneously distributed water at the bed. In some cases, $[P^{c}_{bed}]_{dB}$ exhibits large fluctuations and sharp peaks with widths of from 1 km to several km. |

**STEP 4: Crosschecking and collection of additional information**

If the diagnosis procedures above do not provide convincing results, this step is important.

(i) Compare the results of diagnosis between neighboring areas.
(ii) Check the elevation of the ice sheet surface and the range of $H$ to determine whether the results of diagnosis appear to be reasonable.
(iii) Check the fluctuation of $[P^{c}_{bed}]_{dB}$ along $X$. Irregular rapid fluctuations imply heterogeneously distributed water at the bed.

**STEP 5: Check for features caused by possible error sources**

Possible sources of error
(i) Rapid spatial changes in radiowave attenuation due to spatial changes in the temperature field.
(ii) Rapid spatial changes in radiowave birefringence due to spatial changes in the crystal orientation fabric.
(iii) Fluctuation of $[P^{c}_{bed}]_{dB}$ due to the roughness of bed/substrate interfaces.

These error sources would result in errors in diagnosis with some probability. See text.

**Fig. 8.** Overview of the approach used to diagnose the subglacial conditions using the H-P plot, the X-PH plot, and other information.





TCD
6, 1781–1837, 2012



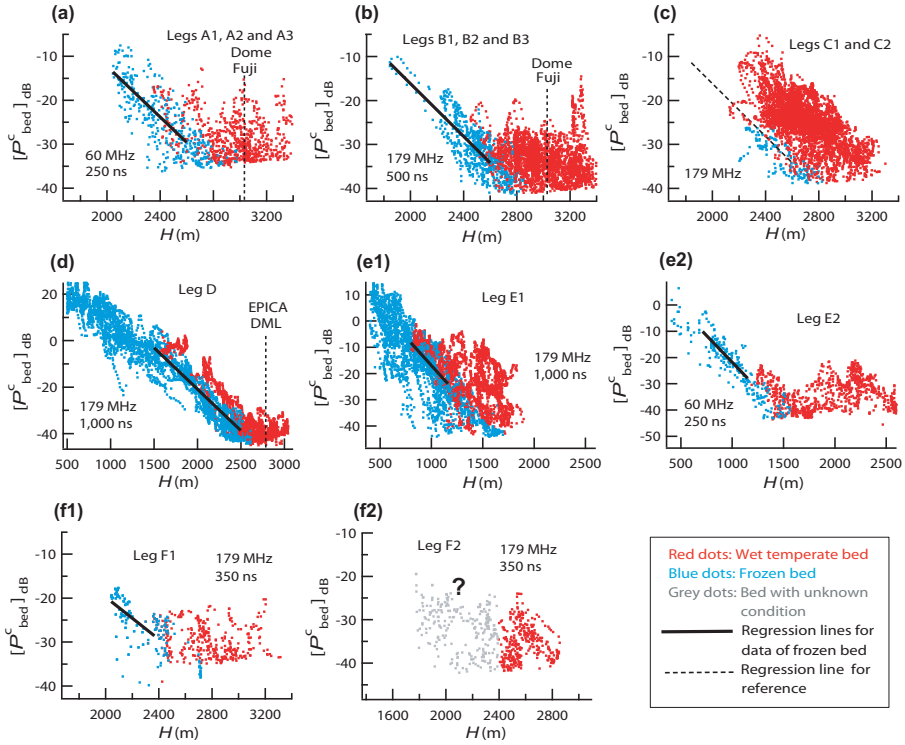


**Fig. 9.** On all data points for the graphs of the H-P plot, the predicted bed condition, i.e., temperate bed or frozen bed, is given. The ID of the leg(s) and the radar settings are indicated on each panel. The panel labels correspond to the names of the legs. The red and blue dots indicate temperate bed and frozen bed, respectively. For leg F2, we were not able to conclusively diagnose some of the data, which are presented in grey. See the text for details.





TCD
6, 1781–1837, 2012



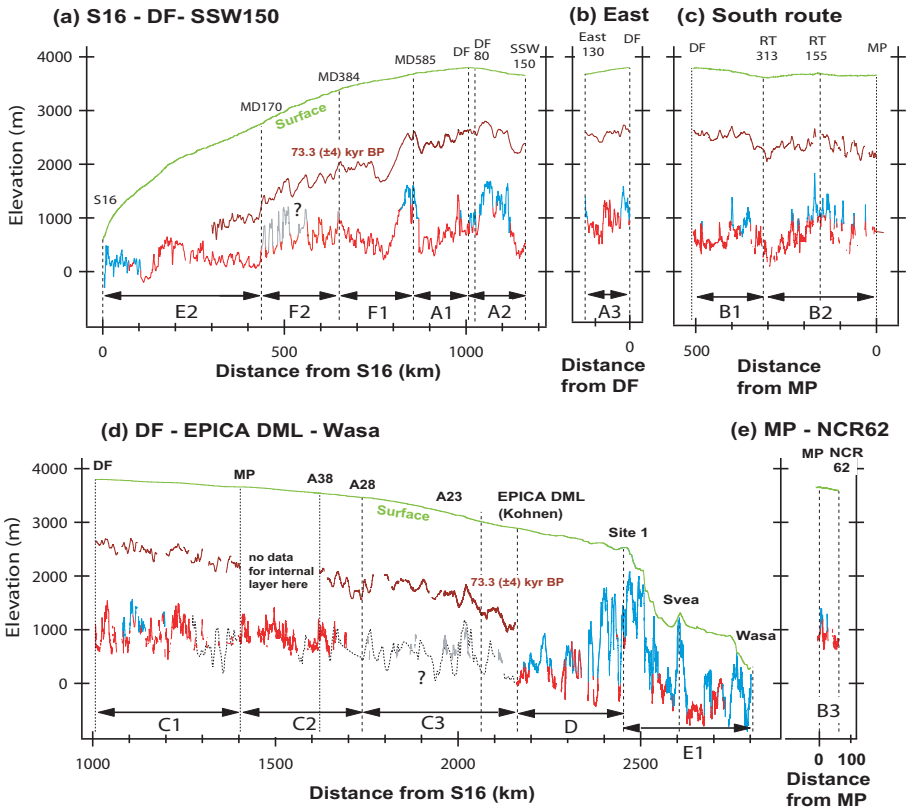


**Fig. 10.** Prediction of temperate bed and frozen bed are shown on the cross-section graph of Fig. 2. The red and blue traces are predicted temperate bed and frozen bed, respectively. The grey areas in legs F2 and C3 indicate that the thickness of the ice was detected although the bed condition remains unknown.





TCD
6, 1781–1837, 2012



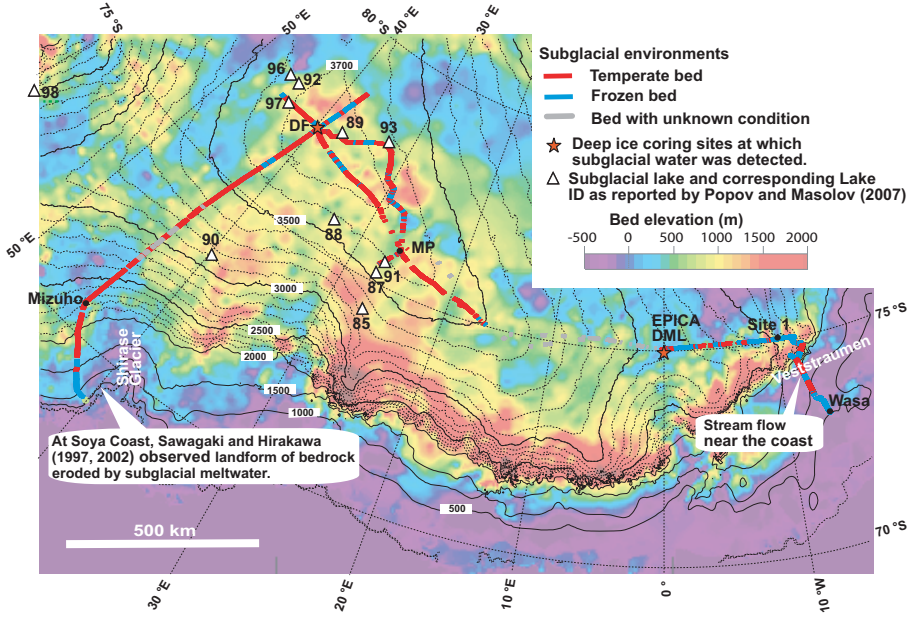


**Fig. 11.** Predicted bed conditions are shown on a bed topography map of DML for the same area shown in Fig. 1. The red and blue dots indicate sites of temperate and frozen bed conditions, respectively. The grey dots were used in legs F2 and C3 for points at which bed condition was unknown. The bed topography map is from the BEDMAP compilation (Lythe et al., 2001), which does not reflect the new data. The bed elevation is shown by the colour scale. Surface elevation is shown by thin black contours. The known information related to subglacial conditions is given in the figure.





TCD
6, 1781–1837, 2012



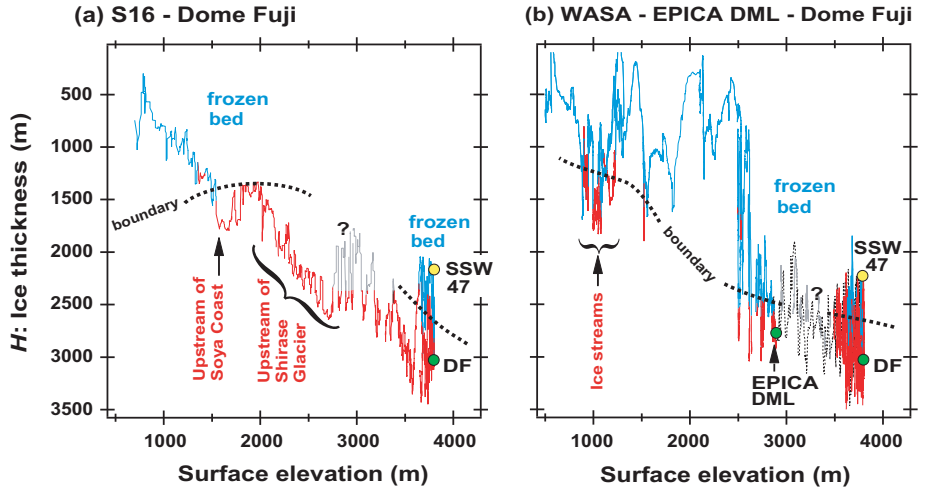


**Fig. 12.** Suggested bed conditions are plotted on graphs of ice thickness *H* (ordinate) versus surface elevation (abscissa). Panels **(a)** and **(b)** are for legs between S16 and the DF area and for legs from Wasa to the DF area, respectively. Frozen dry bed and temperate wet bed are indicated as blue and red traces, respectively. Grey traces indicate unidentified bed conditions. The thin black lines represent published data (Huybrechts et al., 2009). Approximate boundaries between two conditions are indicated by black dotted lines. The locations of two ice coring sites, i.e., Dome Fuji and EPICA DML, are indicated by green symbols. In addition, a candidate location for future ice coring, SSW47, (see Sect. 4.4 of the text) is also indicated.





TCD
6, 1781–1837, 2012



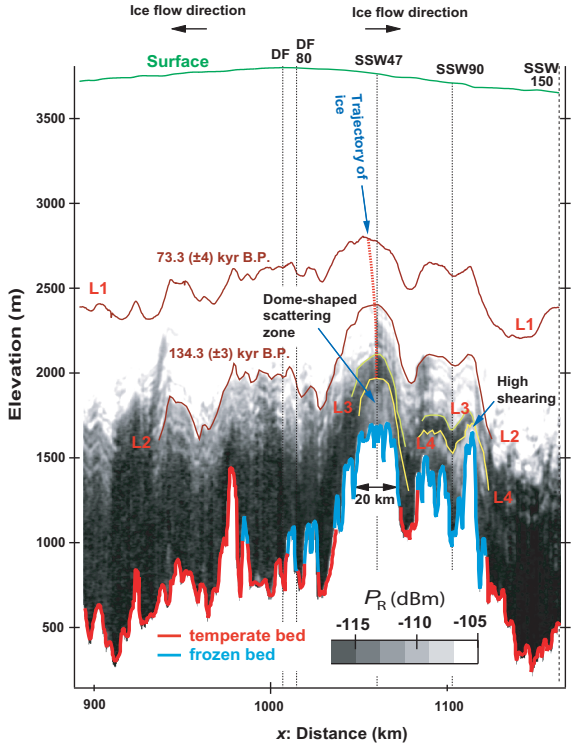


**Fig. 13.** Cross-section of the ice sheet along legs A1 and A2 across DF. The surface elevation, the elevation of four isochrones (englacial reflection layers), and the bed elevation with diagnosed subglacial conditions are shown. Again, blue and red profiles represent inferred frozen dry and temperate wet conditions, respectively. The scattering of radio wave from within ice is also shown in grey scale ranging from −105 dBm to −115 dBm, indicating the scattering of radio waves very deep in the ice sheet. Above subglacial mountains SSW of DF, we find scattering from within very deep ice, which has a dome shape with a width of approximately 20 km. See the text for more details.





TCD
6, 1781–1837, 2012